JOURNAL OF PETROLOGY | VOLUME 43 | NUMBER 12 | PAGES 2305–2338 | 2002

Garnet-field Melting and Late-stage Refertilization in 'Residual' Abyssal Peridotites from the Central Indian Ridge

ERIC HELLEBRAND*, JONATHAN E. SNOW, PETER HOPPE AND ALBRECHT W. HOFMANN

MAX-PLANCK-INSTITUT FÜR CHEMIE, POSTFACH 3060, D-55020 MAINZ, GERMANY

RECEIVED MARCH 22, 2001; REVISED TYPESCRIPT ACCEPTED JUNE 13, 2002

The role of residual garnet during melting beneath mid-ocean ridges has been the subject of many recent investigations. To address this issue from the perspective of melting residues, we obtained major and trace element mineral chemistry of residual abyssal peridotites from the Central Indian Ridge. Many clinopyroxenes have ratios of middle to heavy rare earth elements (MREE/HREE) that are too low to be explained by melting in the stability field of spinel peridotite alone. Several percent of melting must have occurred at higher pressures in the garnet peridotite stability field. Application of new trace element partitioning models, which predict that HREE are compatible in high-pressure clinopyroxene, cannot fully explain the fractionation of the MREE from the HREE. Further, many samples show textural and chemical evidence for refertilization, such as relative enrichments of highly incompatible trace elements with respect to moderately incompatible trace elements. Therefore, highly incompatible elements, which are decoupled from major and moderately incompatible trace elements, are useful to assess late-stage processes, such as melt entrapment, melt–rock reaction and veining. Moderately incompatible trace elements are less affected by such late-stage processes and thus useful to infer the melting history of abyssal peridotites.

KEY WORDS: *abyssal peridotites; mantle melting; garnet*

INTRODUCTION

Mid-ocean ridge basalts (MORB) are the products of partial melting of the upwelling mantle, and form the upper part of the oceanic crust (e.g. Green & Ringwood, 1967; Bottinga & Allègre, 1978; McKenzie, 1984). Petrological, geochemical and experimental evidence as well as thermodynamic considerations suggest that this adiabatic decompression melting is a polybaric process (O'Hara, 1985; Klein & Langmuir, 1987; McKenzie & Bickle, 1988). The depth at which melting begins, however, is intensely debated (Klein & Langmuir, 1987; McKenzie & Bickle, 1988; Langmuir *et al.*, 1992; Shen & Forsyth, 1995), as this has direct implications for the temperature of the upwelling mantle and the thickness of the generated crust. Several geochemical characteristics of MORB are attributed to melting in the presence of residual garnet, suggesting that the depth of onset of melting exceeds ~85 km (Green & Ringwood, 1970; O'Hara *et al.*, 1971; Takahashi, 1986):

(1) high middle to heavy rare earth element ratios (MREE/HREE) occur in melt inclusions in magnesian olivines from Mid-Atlantic Ridge basalts (Sobolev, 1996; Shimizu, 1998).

(2) Examination of combined Lu–Hf and Sm–Nd systematics by Salters & Hart (1989) and Salters (1996) revealed subchondritic Lu/Hf values in MORB, but a long-term Lu/Hf value that is higher than chondritic. These workers explained this so-called Hf paradox by a recent Lu–Hf fractionation during MORB genesis in the presence of garnet.

(3) The generation of excess ^{230}Th in axial MORB glasses from several locations along the mid-ocean ridge system requires garnet in the source (Beattie, 1993; LaTourette *et al.*, 1993; Lundstrom *et al.*, 1995; Bourdon *et al.*, 1996). Furthermore, melt extraction must be almost

*Corresponding author. E-mail: ehelle@mpch-mainz.mpg.de

purely fractional to produce the observed U-series disequilibria, meaning that small melt increments are immediately separated from the residue. However, the melt formed cannot be perfectly extracted from the residue; a very small fraction will probably be retained on grain boundaries or in interstices between minerals. This residual melt porosity has been estimated to be in the range of 0·1–1% (Langmuir *et al.*, 1992; Spiegelman & Elliott, 1993; Lundstrom *et al.*, 2000).

The inferences drawn from trace element melting models depend strongly on the trace element partition coefficients (*D* values) between the silicate melt and the mantle phases clinopyroxene (cpx) and garnet, which accommodate the bulk of the incompatible lithophile trace elements. For the REE, cpx and garnet have highly different partition coefficients. The partition coefficients between garnet and melt increase steadily from highly incompatible for the light REE (LREE) to moderately compatible for the HREE (e.g. Irving & Frey, 1978; Hauri & Hart, 1995; Johnson, 1998). In cpx, LREE are also highly incompatible, whereas MREE and HREE are moderately incompatible (e.g. Hart & Dunn, 1993, and references therein). It is also well known that trace element partition coefficients are not constant throughout the melting column, but vary with pressure, temperature and mineral composition (Gallahan & Nielsen, 1992; Lundstrom *et al.*, 1994; Gaetani & Grove, 1995; Wood & Blundy, 1997; Blundy *et al.*, 1998; Johnson, 1998). Recent experiments and theoretical considerations described by Blundy *et al.* (1998) revealed that HREE are moderately compatible in Na- and Al-rich cpx on the spinel lherzolite solidus. According to that study, high-pressure cpx has partitioning characteristics that are more garnet-like than previously assumed. This would imply that involvement of garnet in MORB generation is drastically reduced (Blundy *et al.*, 1998). Documenting a garnet signature in MORB lavas conclusively is hindered by processes such as magmatic mixing, and polybaric melting.

Studying the residues of partial melting allows us to address this issue from a different, complementary perspective. Residual mantle peridotites are depleted in basaltic components, as a result of melt extraction (Dick *et al.*, 1984; Michael & Bonatti, 1985; Dick, 1989). Normally, the residual rocks from the uppermost mantle are inaccessible because of the overlying 6–7 km thick magmatic crust. At many locations along mid-ocean ridges, however, such mantle melting residues are tectonically exposed on the ocean floor (Aumento & Loubat, 1971; Dick *et al.*, 1984; Cannat, 1993). These so-called abyssal peridotites are commonly highly altered, but contain mineral relicts that preserve primary information about melting and melt extraction. At present, several melting models are used to explain the available abyssal peridotite data. Strong LREE depletions in residual cpx confirm that melt extraction beneath mid-ocean ridges is nearly fractional (Johnson *et al.*, 1990; Johnson & Dick, 1992). Apparently, this disagrees with results from major element modelling using MELTS, which suggests that batch (high-porosity) melting is required to explain the major element composition of abyssal peridotites (Asimow, 1999). However, batch melting has only a minor effect on the fractionation of incompatible trace elements in the residue, i.e. trace element ratios hardly vary as a function of melt fraction produced, in contrast to fractional melting. As an apparent compromise, recent considerations have shown that cpx REE patterns in abyssal peridotites are also consistent with near-fractional melting followed by batch melting or vice versa (Kelemen *et al.*, 1997; Asimow, 1999).

The abyssal peridotite database on which these interpretations are based is small, and restricted mainly to fracture zone peridotites from the very slow-spreading Southwest Indian and America–Antarctica ridges (Johnson *et al.*, 1990; Johnson & Dick, 1992) and two localities in the North Atlantic (Ross & Elthon, 1997) and Pacific oceans (Dick & Natland, 1996). To expand this database towards faster-spreading ridges, we obtained major and trace element data by electron and ion microprobe analysis on fresh primary minerals of vein-free and plagioclase-free peridotites from the intermediate-spreading Central Indian Ridge (CIR).

GEOLOGICAL SETTING

The north–south-trending Central Indian Ridge (CIR) is an intermediate-spreading mid-ocean ridge. Spreading rates, predicted by NUVEL 1 plate velocity model (DeMets *et al.*, 1990), vary from 30 mm/yr (full rate) near the equator to 49 mm/yr at the Rodrigues Triple Junction (RTJ). In contrast to the highly oblique-spreading Southwest Indian Ridge (SWIR), the CIR is characterized by a moderate but variable ridge obliquity (Fig. 1). Between the RTJ at 25°S and Argo Fracture Zone (FZ) at 13°S, spreading is nearly orthogonal (Dyment, 1998). Very few large-offset fracture zones occur in this part of the CIR. The most prominent transform fault is the Marie Celeste FZ (MCFZ) at 17°S, offsetting the CIR by almost 300 km. North of Argo FZ, the CIR trends NNE and spreading is highly oblique (Fig. 1). Here, the CIR is dominated by smaller ridge segments, separated by numerous NE–SW-trending small-offset transform faults. North of 5°S the CIR gradually returns to NNW-trending orthogonal spreading. The NW-trending Carlsberg Ridge is the northern continuation of the CIR and is devoid of fracture zones.

In contrast to most other mid-ocean ridges, few active hotspots have interacted with the ridge in recent times. Only the Réunion hotspot, now located 1100 km west

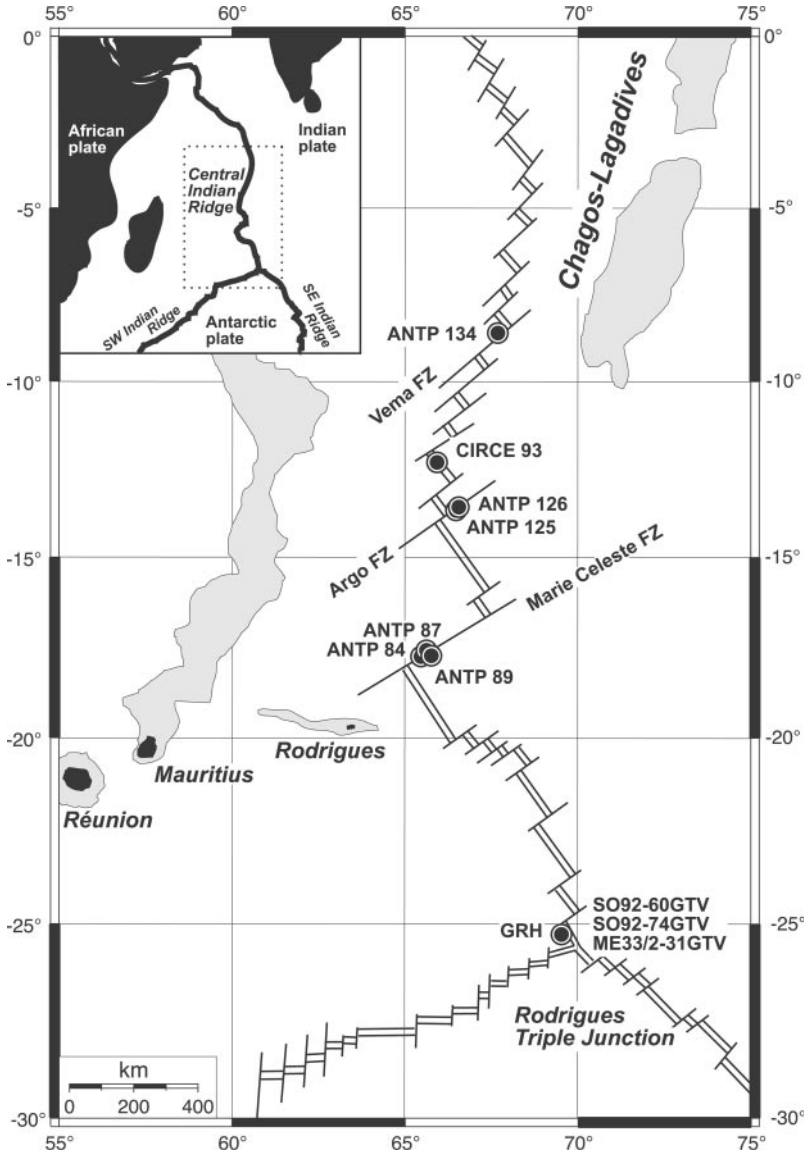

Fig. 1. Bathymetric map of the northwestern part of the Indian Ocean showing the Central Indian Ridge (CIR) and its major transform faults. The grey field encloses the 3000 m isobath and marks the Réunion hotspot track. Numbers refer to sampling locations listed in Table 1. GRH, Green Rock Hill.

of the ridge axis, interacted with the CIR. Around magnetic anomaly 21 (47 Ma), the hotspot crossed the CIR from the Indian to the African plate (Dyment, 1998). The track of the Réunion hotspot can be traced back to the Chagos–Lagadive Ridge on the Indian plate, and finally to India, where it initially produced the Deccan traps ~66 Myr ago (Mahoney, 1988). Despite the large distance to the current Réunion hotspot, several indications suggest a cryptic ridge–hotspot interaction along the CIR near 18–20°S. A broad bathymetric anomaly is observed at the CIR, centred on 19°S, 66°E (Briais, 1995) and the long-wavelength bathymetry varies towards the RTJ. The axial depth of the CIR increases gradually from an average of 3200 m at 20°S to 4000 m at the triple junction (Briais, 1995). Further, a narrow east–west-trending linear structure between Mauritius and the CIR, named Rodrigues Ridge, approaches within 50 km of the axis. Volcanic rocks from Rodrigues Island, the only subaerial expression of this obscure volcanic ridge, are compositionally very similar to those of Réunion and Mauritius (Baxter *et al.*, 1985) and have an age of 1·58–1·30 Ma (McDougall & Chamalaun, 1969). This excludes an origin at the ridge, but supports the hypothesis of Morgan (1978), who suggested channelized asthenospheric flow from the Réunion hotspot towards the CIR to explain the Rodrigues volcanism. Apparently, the

melting region beneath the MCFZ and the neighbouring CIR segments is tapping the same source, as reflected by the enriched MORB geochemistry (Mahoney *et al.*, 1989). A low-velocity signature beneath Réunion–Mauritius and the CIR could reflect a real connection between actual hotspot material and the CIR (Debayle & Leveque, 1997).

Isotopic and trace element data from basalts confirm a currently active ridge–hotspot interaction at the CIR, although the sampling density is poor compared with better-studied mid-ocean ridges such as the East Pacific Rise and the Mid-Atlantic Ridge. It is well known, however, that Indian Ocean MORBs differ in Sr–Nd–Pb isotopic composition from those of the Atlantic and Pacific Ocean (Dupré & Allègre, 1983; Hart, 1984; Rehkämper & Hofmann, 1997). Higher $^{208}Pb/^{204}Pb$ and $^{207}Pb/^{204}Pb$ values at a given $^{206}Pb/^{204}Pb$ value than beneath the Atlantic and Pacific have led to the concept that the sub-Indian Ocean mantle has been enriched by recycled sediments (Rehkämper & Hofmann, 1997), or delaminated subcontinental lithosphere (Schiano *et al.*, 1997). On a regional scale, the MCFZ and the adjacent ridge segment to the south are geochemically anomalous, which agrees with the anomalies seen in the bathymetry. MORB glasses with high $^{87}Sr/^{86}Sr$ values of 0·7030–0·7036 and $^{206}Pb/^{204}Pb$ values of 18·3–18·9 suggest that the MORB source region in this part of the CIR is influenced by an enriched component, despite the distance to the current or past locations of the Réunion hotspot (Mahoney *et al.*, 1989). $Na_{8·0}$, $Fe_{8·0}$ and incompatible trace element concentrations in MORB show large scatter for relatively primitive Mg-number [= molar Mg/(Mg + Fe)] >0·55 (Natland, 1991), suggesting significant heterogeneities in the mantle source beneath the ridge and the MCFZ. In other portions of the CIR, large local variations are absent. The southern part of the CIR appears to be chemically unaffected by the hotspot, and the $Na_{8·0}$ of the basalt also gradually increases from 2·3 at 19°S to 3·0 at the RTJ. This is in accordance with the global correlation between ridge depth and basalt composition (Klein & Langmuir, 1987).

Samples and petrography

Forty abyssal peridotites from 11 stations along the Central Indian Ridge were studied by electron and ion microprobe. The sampling locations are shown in Fig. 1. Most samples were collected during the Scripps Institution of Oceanography expeditions CIRCE and ANTIPODES at Argo, Marie Celeste and Vema fracture zones, and along the CIR axis at 12°S (Engel & Fisher, 1975). Recently, outcropping serpentinized peridotites were sampled by TV-grab at Green Rock Hill (GRH), located off-axis on the western flank of the southernmost CIR segment during cruises SO92 with R.V. *Sonne* in 1994 and ME33/2 with R.V. *Meteor* in 1995, yielding three well-positioned peridotite sample sets from one large peridotite exposure.

Residual peridotites were selected for analysis using the same criteria as Johnson *et al.* (1990), to allow direct comparison between the two datasets. From a total of 40 peridotite samples, 25 are texturallly residual. Fifteen non-residual samples were discarded for this study, because seven peridotites contained minor amounts of plagioclase, and eight were cut by thin (<1 mm) magmatic veins. These non-residual peridotites will be discussed elsewhere. Modal compositions of all residual peridotite samples except those from GRH were determined by point-counting large-format thin sections in a previous study (Dick & Bullen, 1984). For a thorough discussion of the assessment and quality of these data the reader is referred to that publication. The precursor rocks of these CIR serpentinites are spinel peridotites [62·6–90·4% olivine, 9·3–35·1% orthopyroxene (opx), 0–7% clinopyroxene (cpx), 0·04–0·9% spinel] (Table 1). With the exception of two lherzolitic samples from Argo FZ (ANTP126-2 and ANTP126-5) and one axial dunite from 12°S (CIRCE93-2), all studied peridotites are harzburgites. The local modal variability is large, especially for the sample set from the MCFZ. Here, virtually cpx-free harzburgites were collected together with modally more fertile samples. All samples are strongly altered, with estimated degrees of serpentinization between 75 and 95% (Table 1). Despite this intense alteration, which is a common feature of abyssal peridotites, key textural features are largely preserved.

The residual CIR peridotites vary between coarse equigranular and porphyroclastic, which is typical for most mantle rocks (e.g. Mercier & Nicolas, 1975). Overall, the CIR peridotites are not strongly deformed, as indicated by aspect ratios of opx porphyroclasts that rarely exceed 3:1 and the coarse olivine grain size. Subsolidus cooling led to formation of cpx exsolution lamellae in opx porphyroclasts and vice versa, which is common in all abyssal peridotites. Small dynamically recrystallized pyroxenes are usually devoid of such exsolutions. Many samples, particularly all peridotite samples from 12°S, contain textures suggestive of reactive porous flow. Their opx–olivine grain boundaries are lobate but highly irregular. Coarse matrix olivine can be clearly distinguished from relatively fine-grained olivines at opx grain boundaries, where abundant interstitial ($\sim$<30 μm) spinel stringers are precipitated. Although plagioclase or its alteration phase, which is commonly a direct indicator for melt entrapment, is absent in all the selected CIR samples, some of these 'residues' contain textural evidence for incomplete melt extraction. In two harzburgites from 12°S, rare cpx occurs as small ($\sim$20–50 μm wide, 0·1–0·5 mm long) (Fig. 2a), irregular interstitial stringers in the

Table 1: Sampling locations and modal analyses of Central Indian Ridge peridotites

Sample	Position		Modes (vol. %)				% Serpentine
	Latitude	Longitude	ol	opx	cpx	sp	
Vema FZ							
ANTP134-3	8°41·5′S	67°38·0′E	69·6	25·3	4·5	0·6	85
ANTP134-4			78·8	16·2	4·2	0·6	90
ANTP134-5			—	—	—	—	95
ANTP134-7			62·6	35·1	1·3	0·9	95
ANTP134-8			—	—	—	—	95
CIR axis 12°S							
Circe93-2	12°25·0′S	65°56·0′E	90·4	9·3	0·1	0·2	75
Circe93-3			78·5	21·2	0·0	0·3	85
Circe93-4			75·5	21·7	2·2	0·7	80
Circe93-5			77·6	22·1	0·0	0·3	85
Circe93-7			83·1	16·7	0·1	0·1	85
Argo FZ							
ANTP126-2	13°33·7′S	66°30·1′E	70·1	23·4	6·1	0·4	80
ANTP126-5			71·3	20·9	7·0	0·8	85
ANTP125-D5			74·6	20·8	3·7	0·9	85
Marie Celeste FZ							
ANTP84-11	17°39·2′S	65°36·6′E	76·7	19·5	3·7	0·1	85
ANTP87-5	17°35·8′S	65°45·2′E	80·8	17·9	1·0	0·3	95
ANTP87-9			82·7	17·1	0·04	0·14	95
ANTP89-1	17°38·1′S	65°49·0′E	71·3	27·8	0·4	0·4	90
ANTP89-2			76·1	21·2	2·2	0·3	90
ANTP89-5			73·1	21·5	4·9	0·5	75
ANTP89-8			75·8	19·9	3·8	0·3	80
ANTP89-15			85·1	14·4	0·5	0·04	85
ANTP89-17			81·0	16·9	1·9	0·1	90
Green Rock Hill							
ME33/2-31GTV	25°23·7′S	69°45·6′E	70·0	28·0	1·4	0·6	91
SO92-60GTV			74·0	22·8	2·6	0·6	93
SO92-74GTV			74·0	23·5	1·9	0·6	85

olivine matrix, or at olivine–opx grain boundaries. Small interstitial cpx grains are also precipitated on deep embayments into opx at grain boundaries with olivine (Fig. 2b). These textures, which are similar to those described by Seyler *et al.* (2001*b*), suggest that melt entrapment led to cpx precipitation on grain boundaries. Similarly, at Green Rock Hill (GRH) cpx occurs mainly as porphyroclasts or in coarse recrystallized aggregates of cpx and subordinate opx. In these harzburgites fine-grained (<50 μm) interstitial cpx occurs as well, but is very rare. All Vema FZ peridotites have opx dissolution textures similar to those from 12°S. However, they contain variable amounts of medium-grained (80–300 μm), mainly strain-free interstitial cpx. One harzburgite (ANTP134-3) contains a coarse (~2 mm) magmatically twinned cpx (Fig. 2c), located between two coarse opx porphyroclasts. This suggests that melt extraction in these samples was also incomplete. Argo FZ peridotites have similar textures to the GRH harzburgites, but with higher modal cpx. As indicated by the relatively large modal variation, the MCFZ harzburgites show variable textures. Porphyroclastic cpx dominates in the modally more fertile samples. In the modally depleted samples cpx is interstitial, mainly occurring at opx grain boundaries.

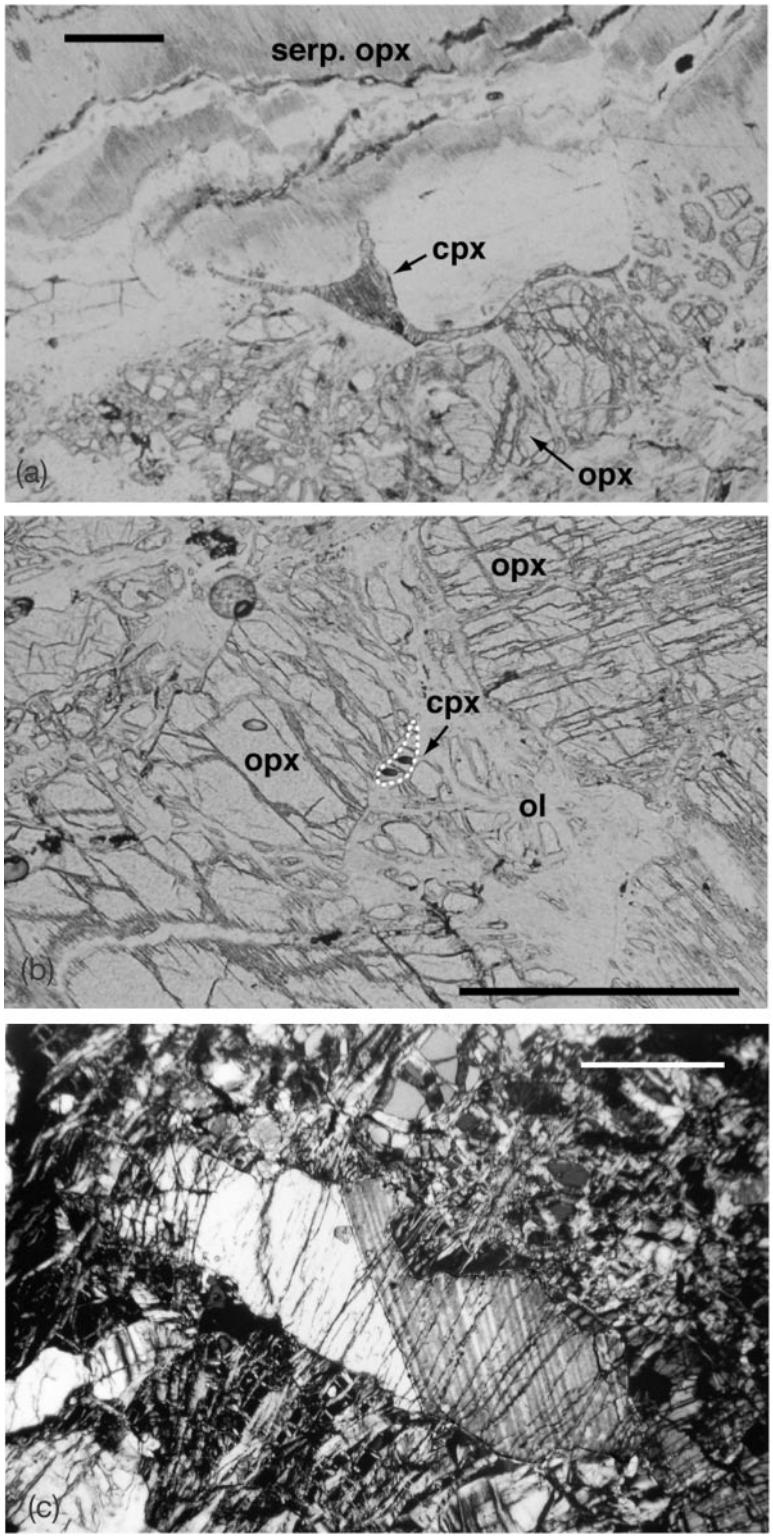

Fig. 2. Photomicrographs of clinopyroxene (cpx) textures, indicative of incomplete melt extraction. (a) Interstitial cpx film (~2 mm long) at an opx–olivine and opx–opx grain boundary in harzburgite CIRCE93-7. Serp, serpentinized. Transmitted light. (b) Small interstitial cpx (highlighted by dashed line) at a deeply embayed opx–olivine grain boundary (CIRCE93-7). The REE pattern of this cpx is hump-shaped, supporting a melt entrapment origin (see discussion). Transmitted light. (c) Coarse magmatic cpx twin surrounded by partly serpentinized olivine in harzburgite ANTP134-3. Crossed polarizers. Scale bar for all micrographs represents 500 μm.

ANALYTICAL METHODS

Anhydrous silicates and spinels were analysed *in situ* for major elements on a five-spectrometer JEOL JXA 8900RL electron probe microanalyser (EPMA) at the University of Mainz using an acceleration potential of 20 kV, a beam current of 20 nA and a spot size of 2 μm. Clinopyroxenes were analysed for trace elements (selected REE and Ti, V, Cr, Sr, Y, Zr) by secondary ion mass spectrometry (SIMS) on a recently upgraded Cameca IMS-3f in Mainz. Spots were selected for ion microprobe analysis after detailed petrographic and electron microprobe study. Only optically clear domains that show no signs of alteration or opx exsolution were analysed. Negative oxygen ions were used as primary ions (accelerating potential of 12·5 kV and 20 nA beam current). The spot size for these operating conditions was 15–20 μm. For very small grains, the beam current was reduced to 10 nA, resulting in a smaller spot size (around 10 μm). Positive secondary ions were extracted using an accelerating potential of 4·5 kV with a 25 eV energy window, a high-energy offset of −80 V, and fully open entrance and exit slits.

Each measurement consisted of a six-cycle routine, where in each cycle the species ^{16}O, ^{30}Si, ^{47}Ti, ^{51}V, ^{52}Cr, ^{88}Sr, ^{89}Y, ^{90}Zr, ^{138}Ba, ^{139}La, ^{140}Ce, ^{146}Nd, ^{147}Sm, ^{153}Eu, ^{157}Gd, ^{163}Dy, ^{167}Er and ^{174}Yb were analysed, in that order. In each cycle, the REE were measured for 30 s, Sr, Zr and Ba for 20 s, Ti, V and Y for 5 s, and the other elements for 1 s. At the beginning of each analysis, the energy distribution of ^{16}O was measured to determine the maximum intensity and the precise location of the 10% low-energy edge of the distribution. The location of this sharp edge can be determined more precisely than the location of relatively broad maximum intensity. Given that $\Delta U_{\text{max-edge}}$ is $\sim +20$ V, the applied high-energy offset is about −100 V from the location of the 10% value of this steep flank. In this way, differences in ion energy as a result of charge build-up from one sample to the next do not affect the energy range of the ions being analysed (Zinner & Crozaz, 1986). Subsequently, peak centres were determined for ^{30}Si, ^{47}Ti, ^{89}Y and ^{163}Dy by scanning the peak in 20 steps across a 1·5‰ wide B-field. The neighbouring masses (Cr and V on Ti, Sr and Zr on Y, and all REE on Dy) were then adjusted to these new peak centres. From one measurement to the next, however, the peak shift was rarely significant (<50 ppm).

For all silicates, ^{30}Si (3·1% isotopic abundance) is used as a reference mass, as the SiO_2 concentration of standards and samples is known from electron microprobe analysis. For each cycle, mass to ^{30}Si ratios were determined after correction for time-dependence of count rates, detector deadtime (20 ms) and background [$\sim 10^{-3}$ c.p.s. (counts per second)]. The average of these ratios was used to calculate the element concentration, multiplying the measured ratios by a constant factor. These so-called sensitivity factors were determined for each element on the well-studied standard glasses KL2-G, ML3B-G, StHs6/80-G, BM90/21-G and ATHO-G (Jochum *et al.*, 2000*a*). For this purpose, a different measurement routine that determines the mass spectrum between 133 and 191 was adopted (Zinner & Crozaz, 1986), referred to below as the 'long routine'. This approach is necessary to obtain accurate sensitivity factors for the REE. Although the applied energy filtering technique (Shimizu *et al.*, 1978) eliminates the effect of most molecular interferences, it is well known that element monoxides can produce significant interferences, particularly on REE (e.g. PrO on Gd). These have to be corrected. The intensity of an interfering oxide is a function of three parameters: the absolute concentration element of the interfering oxide (i.e. shape of the REE pattern), its isotopic abundance, and the oxide/element ratio of the interfering species. In contrast to the short routine described above, the long routine provides an internally consistent method to determine the corrected element/Si ratios and the oxide/element ratio. A detailed description of this iterative data reduction procedure was presented by Zinner & Crozaz (1986).

Owing to the low REE concentrations in clinopyroxenes of residual mantle rocks, the short measurement routine was preferred over the long routine, as the poor counting statistics at the extremely low counting rates caused an unacceptable propagating error and long duration time for a single analysis. Therefore, the short routine used the MO^+/M^+ values obtained by the long routine. Furthermore, six oxides were found to produce significant interferences: $^{137}BaO^+$ interferes with $^{153}Eu^+$, $^{141}PrO^+$ with $^{157}Gd^+$, $^{147}SmO^+$ with $^{163}Dy^+$, $^{151}EuO^+$ with $^{167}Er^+$, and both $^{158}GdO^+$ and $^{158}DyO^+$ with $^{174}Yb^+$, and their MO^+ to M^+ ratios used for the corrections are 0·046, 0·13, 0·06, 0·05, 0·08 and 0·07, respectively (with errors <10%). As all elements of these oxides are free of interferences, they were measured directly, except for Pr, which was calculated as the chondrite-normalized geometric mean of Ce and Nd. This calculated value did not deviate significantly from values determined using the long routine. For the concentrations of Eu, Gd, Dy and Er in a typical LREE-depleted clinopyroxene, these corrections were always <2% of the measured element/Si ratio. For Yb, the correction varied between 3 and 11%, depending on the slope of the REE pattern. In one unusual sample (CIRCE93-7), which is characterized by a hump-shaped REE pattern, the correction on Er and Yb was 6% and 17%, respectively.

The well-studied glass GOR132-G (Jochum *et al.*, 2000*a*) was used as an external standard, as its LREE-depleted pattern is similar to that of the measured

clinopyroxenes. The 1σ values of this standard, as listed in Table 4 (below), account for the propagated errors caused by the interference corrections. The overall accuracy is better than 20% for all REE and better than 12% for all other elements (95% confidence level). It should be noted that in-run precision of the Ce/Yb and Sm/Yb ratios (see discussion) of the samples is independent of sensitivity factors and external standards. The 1σ values for these ratios in GOR132-G are better than 9% for an individual analysis.

To distinguish 'real' counts from background noise at extremely low counting rates, separate background measurements with long counting times between 10 and 30 min were carried out. All reported analyses are corrected for the background, which lies around 10^{-3} (c.p.s.) on average. The background concentration for each element that is based on such a count rate is controlled primarily by the intensity of ^{30}Si, which was $\sim(1{\cdot}0–1{\cdot}3) \times 10^5$ c.p.s. Defining a conservative detection limit at the sixfold background level, this corresponds to values for the REE that range from 0·6 ng/g (La) to 4 ng/g (Sm) (see Table 4, below). This low background is confirmed by a virtually La-free sample ANTP84-11, where only two counts were registered on mass 139 in 12 cycles of 30 s each ($5{\cdot}6 \times 10^{-3}$ c.p.s.).

Some analyses were duplicated with the Cameca IMS-3f ion microprobe at Woods Hole Oceanographic Institution (WHOI), as noted in Table 4. The major difference between the WHOI and MPI measurement routines is that REE and other trace elements (Ti, V, Cr, Sr, Y, Zr) were measured separately with the WHOI ion probe, applying different high-energy offsets of −60 V and −100 V, respectively. The detailed analytical conditions for these measurements have been reported by Johnson *et al.* (1990). Although the general REE patterns are well reproduced (see Fig. 5, below), the HREE concentrations measured at Mainz are 20–30% higher than those measured by the WHOI ion probe. These discrepancies, which have no effect on our conclusions, might stem from the use of different standards and/or application of different interference corrections. The MPI glass standards have a large range of LREE/HREE ratios, thus a large range of interference corrections, and provide internally consistent results. Furthermore, large discrepancies exist between the Woods Hole and the Mainz data for Sr and Zr, for which we do not have a satisfactory explanation. Sensitivity factors, obtained on the glass standards with the MPI ion probe, were identical within <3%. Major element molecular interferences that might occur at very low concentrations can be excluded as well under the stated operating conditions. Finally, it is important to note that the cpx data of the pioneering work of Johnson *et al.* (1990, 1992) were not corrected for possible interferences of MREE oxides on the HREE (K. T. M. Johnson, personal communication, 2001).

RESULTS

Mineral compositions

The mineral major element compositions of all the residual CIR peridotites (Tables 2–6) lie within the range of typical oceanic upper-mantle melting residues (Dick & Bullen, 1984; Dick *et al.*, 1984; Michael & Bonatti, 1985; Dick, 1989). Significant within-sample variations, such as lower Al and Cr content and slightly higher Mg-number in fine-grained strain-free pyroxenes with respect to porphyroclast cores, are also typical features of abyssal peridotites, attributed to subsolidus re-equilibration (Sinton, 1978; Hamlyn & Bonatti, 1980; Tartarotti *et al.*, 1995). However, global melting trends show that with increasing degree of melting, the Al content of pyroxene decreases and silicate Mg-number increases. Therefore, textural relationships are important, because cooling trends cannot easily be distinguished from melting trends (see Fig. 4a). Hence, porphyroclast core compositions were used for comparison, whenever possible. In some samples, however, porphyroclasts were either absent or too intensely altered.

On the basis of whether major element compositional variation is observed within a single dredge haul, two groups can be defined: Group 1 has a narrow range in the mineral chemistry, whereas Group 2 shows larger chemical variations.

Spinel

Spinel Cr-number [= molar Cr/(Cr + Al)] is generally accepted as a sensitive indicator for the extent of melting (Dick & Bullen, 1984), and melt–peridotite reaction (Kelemen *et al.*, 1992). This value increases with increasing degrees of melting. Spinel Cr-number of CIR peridotites ranges from 0·17 for a harzburgite from Marie Celeste FZ, to 0·57 for the axial dunite from 12°S. This corresponds to 3–17% of perfect fractional melting of a depleted mantle starting source (Hellebrand *et al.*, 2001). As extreme serpentinization and weathering in some samples may obscure the presence of very small amounts of plagioclase, titanium content of spinel is used as an additional monitor for this phase. Commonly, the titanium content in spinels of plagioclase-bearing abyssal peridotites is higher than in plagioclase-free melting residues (Dick, 1989; E. Hellebrand, unpublished results, 2002). The majority of all plagioclase-bearing peridotites have spinel TiO_2 contents exceeding 0·2 wt %, which attests to the non-residual nature of most abyssal plagioclase peridotites. In the selected CIR peridotites, all

Table 2: Average major element compositions (in wt %) of spinels of CIR peridotites analysed by electron microprobe

Sample	gr	*n*	TiO_2	Al_2O_3	Cr_2O_3	FeO*	MgO	MnO	NiO	Total	Mg-no.	Cr-no.
Vema FZ												
ANTP134-3	1	1	0·03	43·52	24·58	14·28	17·89	0·13	0·21	100·64	0·734	0·275
ANTP134-5	1	2	0·07	41·43	27·53	12·97	18·45	0·14	0·21	100·79	0·759	0·308
ANTP134-7	1	3	0·07	40·84	28·69	12·34	18·45	0·13	0·24	100·77	0·762	0·320
ANTP134-8	1	2	0·08	42·38	26·83	12·40	18·40	0·16	0·23	100·46	0·758	0·298
CIR 12°S												
Circe93-2	4	10	0·10	40·71	28·87	12·84	18·07	0·16	0·18	100·92	0·747	0·323
Circe93-3	3	5	0·13	35·37	34·47	13·85	16·97	0·19	0·15	101·13	0·719	0·395
Circe93-4	1	3	0·06	41·68	27·34	12·66	18·51	0·15	0·21	100·61	0·763	0·306
Circe93-5	2	4	0·09	25·88	43·86	15·98	15·38	0·23	0·09	101·50	0·680	0·533
Circe93-7	3	6	0·04	35·29	34·32	13·93	17·03	0·2	0·15	100·95	0·724	0·395
Argo FZ												
ANTP126-2	3	6	0·02	48·33	20·45	11·12	19·96	0·13	0·27	100·28	0·800	0·221
ANTP126-5	1	2	0·02	48·5	20·44	10·98	19·89	0·12	0·27	100·21	0·797	0·220
ANTP126-D5	3	6	0·04	48·55	20·53	11·03	19·85	0·11	0·27	100·38	0·795	0·221
Marie Celeste FZ												
ANTP84-11	1	3	0·01	39·17	29·40	14·52	18·08	0·17	0·20	101·55	0·749	0·335
ANTP87-5	1	3	0·02	39·93	27·61	15·85	17·82	0·19	0·22	101·64	0·737	0·317
ANTP87-9	3	6	0·04	34·55	32·16	17·50	17·07	0·18	0·21	101·72	0·721	0·384
ANTP89-1	2	6	0·07	43·30	26·01	12·65	19·09	0·15	0·24	101·51	0·775	0·287
ANTP89-2 (1)	2	4	0·04	45·20	23·57	14·10	18·43	0·15	0·23	101·72	0·745	0·259
ANTP89-2 (2)	1	3	0·18	28·39	40·36	18·17	14·92	0·26	0·09	102·36	0·650	0·488
ANTP89-5	1	2	0·04	51·60	16·29	13·32	19·66	0·15	0·31	101·36	0·775	0·175
ANTP89-8	2	4	0·01	50·03	18·83	12·55	19·83	0·15	0·29	101·70	0·783	0·202
ANTP89-15	3	9	0·07	43·12	26·36	12·90	19·25	0·15	0·24	102·09	0·778	0·291
ANTP89-17	2	5	0·03	43·67	25·64	13·71	18·17	0·17	0·18	101·57	0·740	0·283
Green Rock Hill												
60GTV	1	3	0·09	35·95	33·21	14·59	17·10	0·17	0·20	101·31	0·722	0·383
31GTV	1	2	0·05	35·58	32·07	15·25	16·47	0·19	0·17	99·78	0·708	0·377
74GTV	2	4	0·09	35·09	33·13	15·04	16·01	0·16	0·20	99·72	0·708	0·387

gr, number of spinel grains analysed; *n*, total number of analyses; Mg-number is molar $Mg/(Mg + Fe^{2+})$; Cr-number is molar $Cr/(Cr + Al)$.

Table 3: Average major element compositions (in wt %) of clinopyroxenes of CIR peridotites analysed by electron microprobe

Sample	*n*	SiO_2	TiO_2	Al_2O_3	Cr_2O_3	FeO	MgO	MnO	CaO	NiO	Na_2O	K_2O	Total	Mg-no.
Vema FZ														
ANTP134-3	15:2p3r	51·47	0·14	4·57	1·37	2·35	16·42	0·09	22·19	0·04	0·50	0·01	99·14	0·926
ANTP134-4*	7:2p1i	51·28	0·12	5·05	1·44	2·45	16·65	0·09	21·61	0·04	0·64	0·01	99·38	0·924
ANTP134-5	4:2r	51·68	0·13	4·32	1·36	2·19	16·53	0·09	22·35	0·04	0·52	0·01	99·21	0·931
ANTP134-7	13:1p3i	51·64	0·15	4·51	1·33	2·17	16·49	0·08	22·23	0·04	0·60	0·01	99·26	0·931
ANTP134-8	3:1p	51·11	0·11	5·37	1·54	2·66	16·65	0·08	20·88	0·04	0·61	0·00	99·04	0·918
CIR 12°S														
Circe93-2	14:5i	51·60	0·17	4·25	1·20	2·44	17·52	0·09	21·89	0·05	0·25	0·00	99·44	0·928
Circe93-4	4:1p	50·28	0·10	5·03	1·43	2·51	17·00	0·08	22·24	0·05	0·10	0·01	98·82	0·923
Circe93-7	13:5i	52·59	0·09	3·81	1·54	2·19	17·43	0·10	21·76	0·05	0·66	0·01	100·23	0·934
Argo FZ														
ANTP126-2	11:4r1i	50·79	0·07	5·28	1·14	2·95	17·63	0·09	20·62	0·05	0·27	0·01	98·89	0·914
ANTP126-5	3:1r	51·03	0·05	5·77	1·25	3·04	17·70	0·11	19·83	0·06	0·28	0·01	99·13	0·912
ANTP125-D5	8:2r2i	51·21	0·09	5·23	1·06	2·95	17·79	0·10	20·42	0·05	0·27	0·02	99·19	0·915
Marie Celeste FZ														
ANTP84-11	7:2p2r	50·78	0·02	4·44	1·38	2·72	17·49	0·09	22·76	0·05	0·11	0·01	99·85	0·920
ANTP87-5	7:3i	51·73	0·05	4·42	1·21	3·12	17·99	0·09	21·45	0·06	0·21	0·00	100·33	0·912
ANTP87-9	7:3i	52·05	0·06	4·02	1·28	3·09	17·98	0·09	21·26	0·05	0·37	0·00	100·25	0·912
ANTP89-1	4:2r	50·97	0·18	5·45	1·55	2·47	16·58	0·09	22·01	0·05	0·60	0·01	99·94	0·923
ANTP89-2	10:3r	51·07	0·12	5·24	1·38	2·58	16·66	0·10	22·73	0·04	0·38	0·01	100·31	0·920
ANTP89-5	4:1p	50·53	0·14	6·16	1·23	3·01	16·79	0·12	22·03	0·05	0·27	0·00	100·32	0·909
ANTP89-8	6:2p	50·59	0·13	6·06	1·34	2·74	16·53	0·11	22·50	0·04	0·30	0·00	100·34	0·915
ANTP89-15	8:2r2i	51·18	0·18	5·17	1·50	2·45	16·83	0·09	22·35	0·05	0·56	0·00	100·35	0·925
ANTP89-17	8:3r	51·14	0·07	4·73	1·34	2·52	17·24	0·10	22·94	0·06	0·07	0·00	100·2	0·924
Green Rock Hill														
31GTV	4:1p1i	51·87	0·08	4·63	1·35	2·85	17·34	0·08	20·54	0·05	0·03	0·01	98·82	0·916
60GTV	18:3p	51·17	0·10	4·38	1·36	2·85	17·94	0·09	21·30	0·05	0·03	0·01	99·27	0·918
74GTV	21:2p2r2i	52·12	0·08	4·33	1·32	3·03	18·03	0·09	21·16	0·04	0·04	0·01	100·25	0·914

n, number of analyses: p, porphyroclast; r, recrystallized px aggregate; i, interstitial (e.g. 8:2p2i means eight analyses on four grains: two porphyroclasts and two interstitial grains).
*Analyses taken ~40 mm away from crosscutting magmatic veinlet.

Table 4: Trace element concentrations (in μg/g) of CIR peridotite clinopyroxenes

Sample	*n*	Lab.	Ti	±	Sr	±	Y	±	Zr	±	La	±	Ce	±
ANTP134-3	2	MPI	790	10*	0·63	0·02	6·2	0·1	0·62	0·03	0·0014	0·0008	0·014	0·004
	2	WHOI	668		1·35		6·0		1·0				0·016	
ANTP134-4†	3	MPI	657	4	0·88	0·02	5·7	0·1	0·54	0·02	0·0023	0·0007	0·036	0·004
	3	WHOI	628		1·07		5·8		1·0				0·035	
ANTP134-7	4	WHOI	858		1·30		6·5		1·6				0·025	
ANTP134-8	1	MPI	601	19	0·65	0·02	4·7	0·2	0·47	0·03	0·0018	0·0013	0·024	0·005
	3	WHOI	641		0·98		6·1		1·2				0·033	
CIRCE 93-2	2	MPI	965	3	1·19	0·02	5·4	0·1	0·40	0·01	0·014	0·003	0·028	0·004
	2	WHOI	825		1·60		4·8		0·76					
CIRCE 93-4	2	MPI	551	2	0·44	0·02	5·0	0·1	0·19	0·01	0·003	0·0016	0·013	0·003
	2	WHOI	451		1·18		5·1		0·53				0·016	
CIRCE 93-7	2	MPI	601	4	3·24	0·11	4·2	0·1	3·5	0·04	0·015	0·002	0·095	0·006
ANTP126-2	2	MPI	391	2	0·54	0·02	4·5	0·1	0·21	0·01	0·009	0·002	0·049	0·004
ANTP126-5	2	MPI	388	2	0·47	0·01	4·6	0·1	0·17	0·01	0·01	0·002	0·045	0·005
	2	WHOI											0·041	
ANTP125-D5	2	MPI	516	2	0·58	0·01	5·2	0·1	0·17	0·01	0·005	0·001	0·02	0·003
	2	WHOI											0·02	
ANTP84-11	4	MPI	130	1	0·19	0·01	2·0	0·1	0·07	0·005	b.d.		0·0023	0·0006
ANTP87-5	2	MPI	259	2	0·25	0·01	2·8	0·1	0·08	0·006	0·0025	0·0007	0·0018	0·0009
ANTP87-9	2	MPI	345	2	0·48	0·02	3·8	0·1	0·11	0·011	0·005	0·002	0·007	0·002
ANTP89-1	2	MPI	913	4	0·72	0·02	6·8	0·1	0·78	0·02	0·0024	0·0008	0·013	0·002
ANTP89-2	2	MPI	767	3	0·40	0·03	6·7	0·1	0·28	0·01	0·0019	0·0008	0·006	0·002
ANTP89-5	3	MPI	791	3	0·27	0·01	7·5	0·1	0·21	0·01	0·001	0·0004	0·005	0·001
ANTP89-8	2	MPI	817	4	0·29	0·01	7·1	0·1	0·26	0·01	0·003	0·001	0·006	0·002
ANTP89-15	4	MPI	1419	3	0·63	0·01	7·2	0·1	0·95	0·02	0·0015	0·0004	0·008	0·001
ANTP89-17	4	MPI	575	2	0·33	0·01	4·2	0·1	0·13	0·005	0·014	0·002	0·013	0·001
31GTV	2	MPI	523	6	0·39	0·02	3·4	0·1	0·16	0·01	0·002	0·0014	0·004	0·003
60GTV	1	MPI	500	4	0·42	0·01	3·5	0·1	0·13	0·008	0·005	0·0009	0·017	0·001
74GTV	3	MPI	460	3	0·29	0·01	3·2	0·1	0·12	0·006	0·0013	0·0005	0·003	0·0008
GOR132-G	25	MPI	1705	86‡	15·7	0·88	13·2	0·6	10·3	0·55	0·087	0·009	0·4	0·028
REE d.l.		MPI									0·0006		0·0007	

Table 4: continued

Sample	Nd	±	Sm	±	Eu	±	Gd	±	Dy	±	Er	±	Yb	±
NTP134-3	0·24	0·03	0·34	0·04	0·14	0·011	0·66	0·04	1·22	0·06	0·84	0·06	0·86	0·04
	0·25		0·25		0·12				0·86		0·62		0·56	
ANTP134-4†	0·26	0·02	0·27	0·02	0·13	0·009	0·68	0·03	1·09	0·04	0·73	0·04	0·83	0·03
	0·31		0·3		0·12				0·78		0·55		0·57	
ANTP134-7	0·28		0·25		0·12				0·85		0·59		0·56	
ANTP134-8	0·19	0·03	0·19	0·03	0·08	0·011	0·65	0·06	0·93	0·1	0·54	0·05	0·58	0·05
	0·29		0·26		0·14				0·87		0·56		0·62	
CIRCE 93-2	0·06	0·01	0·12	0·02	0·06	0·005	0·42	0·03	0·75	0·04	0·64	0·03	0·72	0·03
	0·12		0·14		0·07				0·64		0·51		0·49	
CIRCE 93-4	0·11	0·02	0·11	0·01	0·05	0·005	0·37	0·03	0·89	0·06	0·63	0·03	0·74	0·03
	0·13		0·14		0·06				0·85		0·6		0·58	
CIRCE 93-7	0·5	0·02	0·46	0·03	0·21	0·009	0·84	0·03	0·84	0·05	0·44	0·02	0·53	0·03
ANTP126-2	0·04	0·01	0·07	0·01	0·04	0·004	0·25	0·02	0·73	0·03	0·61	0·03	0·66	0·03
ANTP126-5	0·06	0·01	0·07	0·02	0·04	0·006	0·34	0·02	0·74	0·04	0·62	0·03	0·75	0·04
	0·09		0·09		0·05				0·61		0·47		0·57	
ANTP125-D5	0·05	0·008	0·13	0·02	0·06	0·005	0·39	0·02	0·94	0·04	0·71	0·03	0·84	0·03
	0·08		0·12		0·08				0·76		0·54		0·62	
ANTP84-11	0·005	0·003	0·009	0·002	0·003	0·001	0·06	0·007	0·29	0·02	0·29	0·02	0·4	0·02
ANTP87-5	b.d.		0·03	0·009	0·02	0·003	0·13	0·02	0·42	0·03	0·46	0·04	0·49	0·02
ANTP87-9	0·02	0·007	0·04	0·009	0·04	0·005	0·22	0·02	0·56	0·06	0·47	0·03	0·59	0·03
ANTP89-1	0·21	0·02	0·3	0·02	0·13	0·008	0·76	0·04	1·33	0·06	0·84	0·03	0·95	0·04
ANTP89-2	0·06	0·01	0·16	0·02	0·1	0·008	0·55	0·04	1·22	0·06	0·84	0·04	0·91	0·04
ANTP89-5	0·13	0·01	0·23	0·02	0·13	0·008	0·73	0·03	1·38	0·05	0·95	0·03	1·08	0·03
ANTP89-8	0·12	0·02	0·21	0·03	0·13	0·009	0·75	0·05	1·33	0·05	0·97	0·04	0·99	0·04
ANTP89-15	0·17	0·01	0·21	0·01	0·13	0·005	0·71	0·02	1·26	0·03	0·93	0·03	0·92	0·02
ANTP89-17	0·012	0·003	0·06	0·01	0·04	0·003	0·24	0·01	0·64	0·02	0·57	0·02	0·72	0·02
31GTV	0·04	0·008	0·06	0·02	0·03	0·005	0·23	0·02	0·61	0·04	0·43	0·03	0·58	0·03
60GTV	0·03	0·006	0·09	0·008	0·04	0·004	0·27	0·02	0·6	0·03	0·43	0·02	0·58	0·02
74GTV	0·02	0·004	0·04	0·006	0·02	0·002	0·18	0·01	0·39	0·02	0·33	0·02	0·33	0·02
GOR132-G	0·73	0·058	0·55	0·048	0·28	0·021	1·27	0·1	2·34	0·2	1·54	0·11	1·53	0·11
REE d.l.	0·003		0·004		0·001		0·004		0·002		0·003		0·001	

MPI, Max-Planck-Institut für Chemie; WHOI, Woods Hole Oceanographic Institution; REE d.l., REE detection limit (6 × background).
*For all samples: weighted mean (internal) error.
†Analyses taken ~40 mm away from crosscutting magmatic veinlet.
‡1 standard deviation (external error).

Table 5: Average major element compositions (in wt %) of orthopyroxenes of CIR peridotites analysed by electron microprobe

Sample	*n*	SiO_2	TiO_2	Al_2O_3	Cr_2O_3	FeO	MgO	MnO	CaO	NiO	Na_2O	Total	Mg-no.
Vema FZ													
ANTP134-3	6	54·38	0·05	3·97	0·87	5·67	33·13	0·13	1·27	0·09	0·03	99·59	0·912
ANTP134-4*	4	54·32	0·05	4·14	0·91	5·54	32·89	0·12	1·75	0·10	0·04	99·85	0·914
ANTP134-5	2	54·35	0·04	4·05	0·91	5·49	33·18	0·09	1·39	0·11	0·01	99·63	0·915
ANTP134-8	2	54·05	0·05	4·26	0·98	5·39	32·44	0·13	2·10	0·09	0·03	99·51	0·915
CIR 12°S													
Circe93-2	4	54·50	0·06	3·84	0·93	5·38	32·94	0·13	2·06	0·10	0·00	99·94	0·916
Circe93-3	2	55·13	0·09	3·17	0·93	5·08	33·46	0·12	1·62	0·10	0·06	99·73	0·922
Circe93-4	2	53·58	0·06	4·10	1·02	5·48	32·59	0·17	2·45	0·11	0·03	99·58	0·914
Circe93-5	2	56·13	0·04	1·76	0·81	4·99	34·48	0·14	1·47	0·09	0·05	99·97	0·925
Circe93-7	6	55·83	0·02	2·87	0·83	5·14	33·99	0·12	1·82	0·10	0·06	100·79	0·922
Argo FZ													
ANTP126-2	4	54·04	0·04	4·10	0·73	5·63	32·69	0·12	1·94	0·10	0·04	99·41	0·912
ANTP126-5	2	54·28	0·01	4·70	0·91	5·67	32·59	0·12	1·56	0·11	0·02	99·96	0·911
ANTP125-D5	4	53·97	0·03	4·57	0·78	5·71	32·52	0·15	1·94	0·10	0·01	99·78	0·910
Marie Celeste FZ													
ANTP84-11	3	54·58	0·01	3·31	0·75	6·15	33·84	0·15	1·66	0·09	0·00	100·55	0·907
ANTP87-5	2	54·96	0·01	3·54	0·75	5·75	33·38	0·13	1·94	0·09	0·01	100·53	0·912
ANTP87-9	4	55·13	0·05	2·89	0·91	5·54	33·85	0·13	2·13	0·09	0·08	100·79	0·916
ANTP89-1	1	53·81	0·06	4·48	1·06	5·21	31·39	0·11	3·59	0·08	0·06	99·87	0·915
ANTP89-2	9	54·37	0·04	4·36	0·95	5·68	33·15	0·14	2·43	0·10	0·05	101·27	0·912
ANTP89-5	3	53·62	0·03	5·19	0·87	6·34	32·62	0·13	1·47	0·10	0·04	100·42	0·902
ANTP89-8	1	53·90	0·03	4·81	0·85	5·87	33·08	0·15	1·97	0·12	0·02	100·80	0·909
ANTP89-15	3	54·39	0·04	4·18	0·97	5·85	34·13	0·13	1·23	0·10	0·02	101·05	0·912
ANTP89-17	3	54·37	0·02	3·95	0·94	6·03	33·07	0·14	2·16	0·10	0·02	100·79	0·907

n, number of analyses; Mg-number is molar $Mg/(Mg + Fe^{2+})$.
*Analyses taken ~40 mm away from crosscutting magmatic veinlet.

Table 6: Average major element compositions (in wt %) of olivines of CIR peridotites analysed by electron microprobe

Sample	*n*	SiO_2	TiO_2	Al_2O_3	Cr_2O_3	FeO	MgO	MnO	CaO	NiO	Total	Mg-no.
Vema FZ												
ANTP134-3	5	40·15	0·00	0·00	0·01	8·56	50·70	0·13	0·02	0·39	99·98	0·913
ANTP134-4*	6	40·48	0·01	0·01	0·01	8·52	51·06	0·12	0·02	0·38	100·62	0·914
ANTP134-5	2	40·00	0·00	0·00	0·02	8·44	51·46	0·11	0·05	0·39	100·47	0·916
ANTP134-8	2	40·26	0·01	0·01	0·02	8·47	50·51	0·12	0·05	0·38	99·86	0·914
CIR 12° S												
Circe93-2	6	40·27	0·01	0·00	0·02	8·62	51·10	0·11	0·05	0·37	100·55	0·914
Circe93-3	10	40·50	0·01	0·00	0·01	7·95	51·28	0·12	0·03	0·39	100·30	0·920
Circe93-4	3	40·09	0·00	0·00	0·00	8·66	50·76	0·13	0·06	0·38	100·10	0·913
Circe93-5	4	40·61	0·01	0·00	0·01	7·87	51·42	0·11	0·05	0·37	100·47	0·921
Circe93-7	4	40·81	0·01	0·01	0·08	7·87	51·73	0·12	0·03	0·40	101·08	0·921
Argo FZ												
ANTP126-2	3	39·86	0·01	0·01	0·03	9·04	50·47	0·13	0·10	0·38	100·04	0·909
ANTP126-5	3	40·20	0·00	0·01	0·02	9·01	50·40	0·14	0·05	0·38	100·22	0·909
ANTP126-D5	2	40·30	0·02	0·03	0·00	8·97	50·33	0·12	0·10	0·38	100·26	0·909

n, number of analyses; Mg-number is molar $Mg/(Mg + Fe^{2+})$.
*Analyses taken ~40 mm away from crosscutting magmatic veinlet.

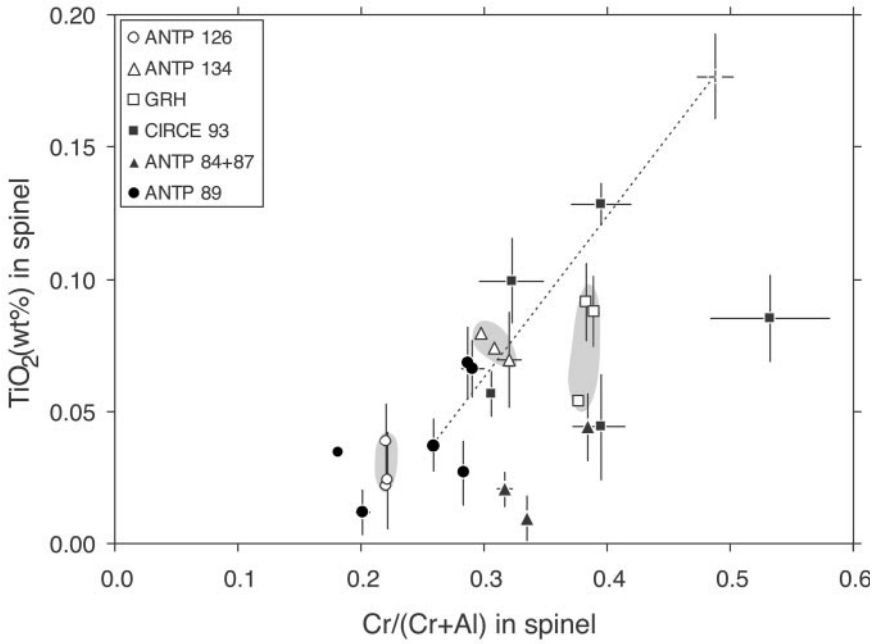

Fig. 3. Spinel TiO_2 content vs spinel Cr-number of CIR residual peridotites. Open symbols, Group 1 samples; filled symbols, Group 2 samples. The low Ti content supports that all studied CIR samples are plagioclase-free. Error bar is 1 SD to illustrate the within-sample variation of Group 2 peridotites. This error bar is smaller than the symbol size for most Group 1 samples. Dashed line connects two chemically distinct spinels in sample ANTP89-2.

titanium contents are well below 0·2 wt % TiO_2. In Fig. 3 the average spinel Cr-number of each sample is plotted versus its titanium content. The error bar (1σ) reflects the analytical uncertainty rather than within-sample inhomogeneity, because of the low absolute variation in Ti. Error bars on Cr-number are seen only in some Group 2 samples, indicating that in these samples heterogeneity also exists on thin-section scale.

Group 1 consists of peridotites from Argo FZ (ANTP126 samples), Green Rock Hill (GTV samples) and Vema FZ (ANTP134 samples). Spinels from the first two localities have constant Cr-number of 0·22 and 0·38, respectively. Limited scatter is observed in the spinels of the four Vema FZ harzburgites, with Cr-number between 0·27 and 0·33. Two vein-bearing peridotites from this dredge haul reach Cr-number of 0·27 far away from the magmatic vein, and 0·39 close to the crosscutting vein. This shows that the crosscutting magmatic veins have produced a small reaction zone in which the spinel compositions were modified. More than 2 cm away from this vein, spinel compositions show normal constant values (Hellebrand *et al.*, 1999).

Group 2 consists of the axial peridotites from 12°S (CIRCE93 samples) and the samples from Marie Celeste FZ (dredges ANTP84, -87 and -89). The Cr-number of the modally depleted 12°S peridotites ranges from 0·29 for 'cpx-rich' harzburgite CIRCE93-4 to 0·57 for the cpx-free dunite CIRCE93-5. Further, all samples are heterogeneous on thin-section scale as indicated by the error bars in Fig. 3. In CIRCE93-2 the Cr-number ranges from 0·30 to 0·36 and CIRCE93-5 has two distinct grains of Cr-number 0·49 and 0·57, respectively. These samples show no indications for the presence of plagioclase or magmatic dykelets, and neither is there any sign of Al-bearing alteration phases, such as chlorite.

Dredge ANTP89 from Marie Celeste FZ consists of six texturally residual peridotites, of which the two most cpx-rich (ANTP89-5, ANTP89-8) have the lowest Cr-number (0·17 and 0·20, respectively). Three samples (ANTP89-1, ANTP89-15, ANTP89-17) have constant Cr-number of 0·28–0·30. The highest Ti concentration of all CIR samples was measured in sample ANTP89-2, which is compositionally very heterogeneous. Two spinel grains have Cr-number of 0·26 and TiO_2 concentrations of 0·04 wt %, and one interstitial grain, 2 cm away from the other two grains, reaches high Cr-number of 0·49 and TiO_2 of 0·18 wt %. In Fig. 3, a dashed line connects these points. Although this sample matched all selection criteria of a residual sample, it appears not to be truly residual and will be discussed below in more detail. Residual peridotites from dredge ANTP84 and -87 consist of one and two samples, respectively, and therefore their within-dredge variations cannot be discussed.

Clinopyroxene

Major elements

The grouping into dredge hauls with constant and variable compositions cannot be strictly applied to pyroxenes, because these show within-sample variability depending on grain size. This may partly be the result of previously mentioned subsolidus cooling effects.

However, in Group 1 all clinopyroxenes from one dredge do show similar limited compositional scatter (Fig. 4). The three Argo FZ peridotites (ANTP126-2, ANTP126-5, ANTP126-D5) have nearly identical average cpx compositions, which agrees well with their relatively fertile modal compositions. Clinopyroxene porphyroclasts in all Green Rock Hill harzburgites (60GTV, 74GTV, 31GTV) are characterized by low TiO_2 concentrations at intermediate Al_2O_3 content. With the exception of the ultra-depleted Hess Deep harzburgites (Dick & Natland, 1996), which were generated in a fast-spreading environment, the GRH clinopyroxenes have the lowest sodium concentrations ever reported along a mid-ocean ridge. The residual Vema FZ peridotites (ANTP134-3, ANTP134-5, ANTP134-7, ANTP134-8) have variable cpx compositions, as already suggested by their variable spinel Cr-number. Sample ANTP134-3, in which a coarse magmatic cpx twin is preserved, has the lowest sodium abundance of the Vema samples. The composition of the twinned cpx does not deviate from other cpx grains in this sample.

In Group 2, the variation in cpx chemistry is much larger than in Group 1 (Fig. 4). Although only three out of five peridotites (CIRCE93-2, CIRCE93-4, CIRCE93-7) from the CIR axis at 12°S contain cpx, each one has an entirely different composition. The cpx porphyroclasts in CIRCE93-4 are characterized by high Mg-number and low TiO_2 and Na_2O concentrations. The interstitial cpx grains of the modally depleted samples CIRCE93-2 and CIRCE93-7 appear more depleted than the porphyroclasts of CIRCE93-4, as suggested by their high Mg-number and low TiO_2 contents. Sodium concentrations of these samples show a contrasting behaviour. In sample CIRCE93-2, sodium is slightly elevated, whereas the otherwise depleted signature of CIRCE93-7 is accompanied by strong sodium enrichments (Na_2O 0·66 wt %). Clinopyroxene compositions from dredge ANTP89 harzburgites cover a broad spectrum. The two 'cpx-rich' harzburgites (ANTP89-5 and ANTP89-8) that have lowest spinel Cr-number have similarly fertile cpx compositions. Their intermediate sodium and titanium concentrations, however, are lower than those of modally very depleted samples ANTP89-1 and ANTP89-15. Clinopyroxene porphyroclasts in ANTP84-11 have the lowest titanium concentrations of all studied samples (0·03 wt % TiO_2), very similar to the depleted cpx from the Bouvet FZ on the Southwest Indian Ridge, close to the Bouvet hotspot (Johnson *et al.*, 1990).

Trace elements

Clinopyroxene REE patterns of Group 1 and Group 2 peridotites are shown in Fig. 5 and listed in Table 4. Significant texture-dependent variation between small neoblasts and porphyroclast cores or rims within a single sample was not observed. In the REE diagrams, the abyssal peridotite field after Johnson *et al.* (1990), which includes only cpx data from the very slow-spreading Southwest Indian and America–Antarctica ridges, is shown for comparison.

Variation-based grouping of the CIR peridotites is also reflected by their cpx trace element signatures, although the spread in Group 2 is limited. Group 1 samples from Argo FZ, GRH and Vema FZ, which all have identical within-dredge major element compositions, also have trace element compositions that are identical within error (Fig. 5a–c). All samples plot in the most depleted part of the abyssal peridotite field and have very low HREE concentrations. Vema FZ peridotites appear to be the most fertile and have the highest MREE to HREE concentrations of Group 1 (Fig. 5c). Their flat MREE to HREE patterns are accompanied by steeply plunging LREE. The Argo FZ samples, on the other hand (Fig. 5a), have more gradually decreasing patterns from HREE to LREE, and their La and Ce abundances are higher than in the clinopyroxenes of the Vema FZ. Despite the absence of any nearby hotspot in the vicinity of the Rodrigues Triple Junction, the Green Rock Hill peridotites (Fig. 5b) are as depleted in REE as the most depleted harzburgite from the hotspot-influenced Bouvet FZ, which is in good agreement with their extremely low sodium concentrations. The minor La inflections in samples 31GTV and 74GTV were measured in four out of five analyses, indicating that they are not analytical artefacts or local effects.

The most remarkable feature of Group 2 (CIR axis 12°S, and Marie Celeste FZ) is the ultra-depleted clinopyroxene composition of sample ANTP84-11 (Fig. 5e). The clinopyroxenes of this sample have four- to sixfold lower LREE to MREE concentrations than those from hotspot-near Bouvet FZ (Johnson *et al.*, 1990). Further, sample ANTP84-11 has the lowest Sr, Zr and Ti concentrations reported for cpx in abyssal peridotites. The titanium concentrations measured by ion probe agree well with those of the electron microprobe (average $Ti_{EPMA}/Ti_{Ion} \sim 1{\cdot}01$). The two cpx-poor harzburgites from dredge ANTP87 have similarly depleted patterns compared with the Bouvet FZ cpx, but both have slight LREE inflections (Fig. 5e). With the exception of sample ANTP89-17, clinopyroxenes in ANTP89 peridotites show very similar REE patterns (Fig. 5f). Of the entire

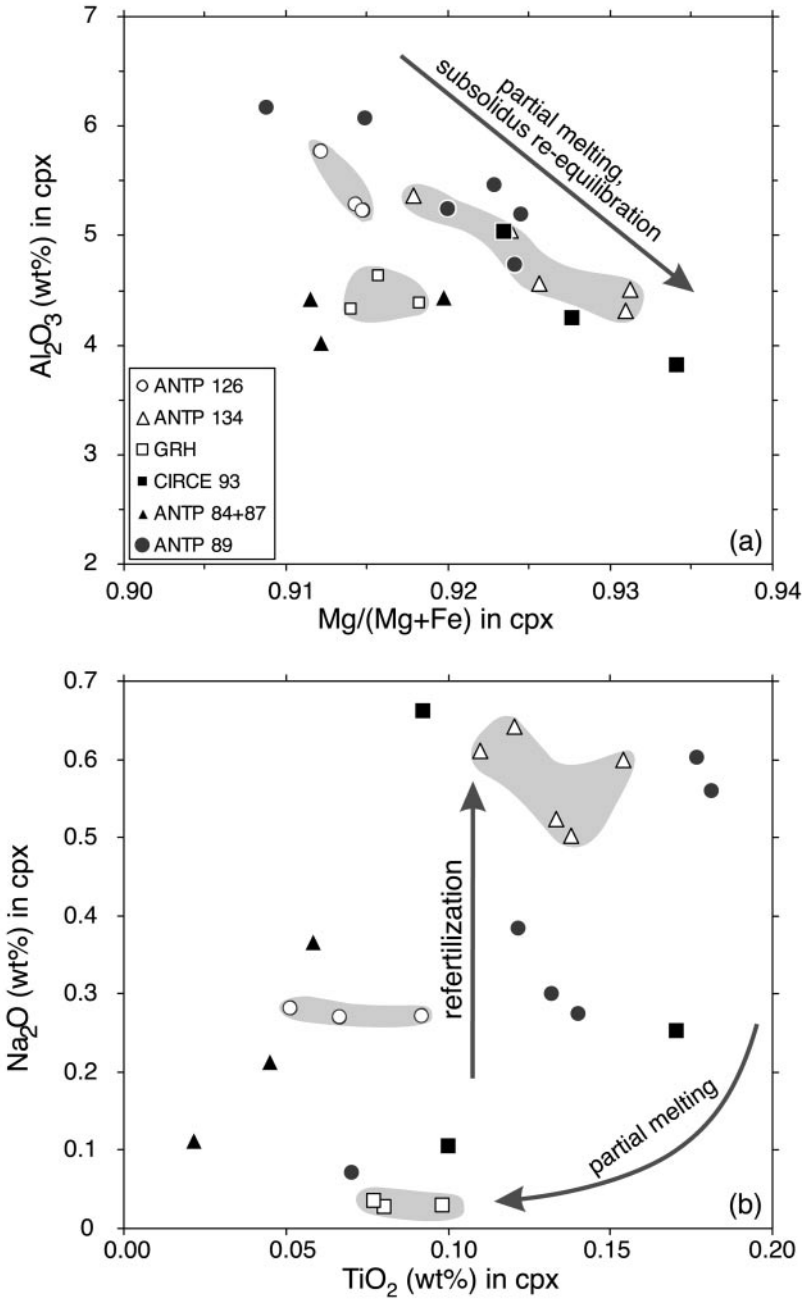

Fig. 4. (a) Al_2O_3 vs Mg-number in cpx. Al decreases and Mg-number increases during partial melting. Some of the scatter may be due to superimposed subsolidus cooling effects. (b) Na_2O vs TiO_2 in cpx. Despite their residual character, a melting trend is absent, which might result from late-stage Na re-enrichment. Symbols as in Fig. 3.

CIR sample set, they have the highest HREE concentrations ($Yb_N \sim 5$). Their average REE pattern is very similar to that of the Vema FZ peridotites, but with significantly lower Ce concentrations. Harzburgite ANTP89-17 has a deviating REE pattern that is almost identical to the most depleted cpx from Bouvet FZ (Johnson *et al.*, 1990), but is characterized by a strong LREE inflection.

Two out of three cpx-bearing CIR 12°S peridotites (samples CIRCE93-2 and CIRCE93-4) have identical trace element compositions (Fig. 5d), except for the La and Ce enrichment in CIRCE93-2. Most uncommon is the hump-shaped pattern of CIRCE93-7, with the highest LREE to MREE and among the lowest Yb concentrations of the CIR samples. The pattern resembles the hump-shaped REE patterns of clinopyroxenes in peridotite

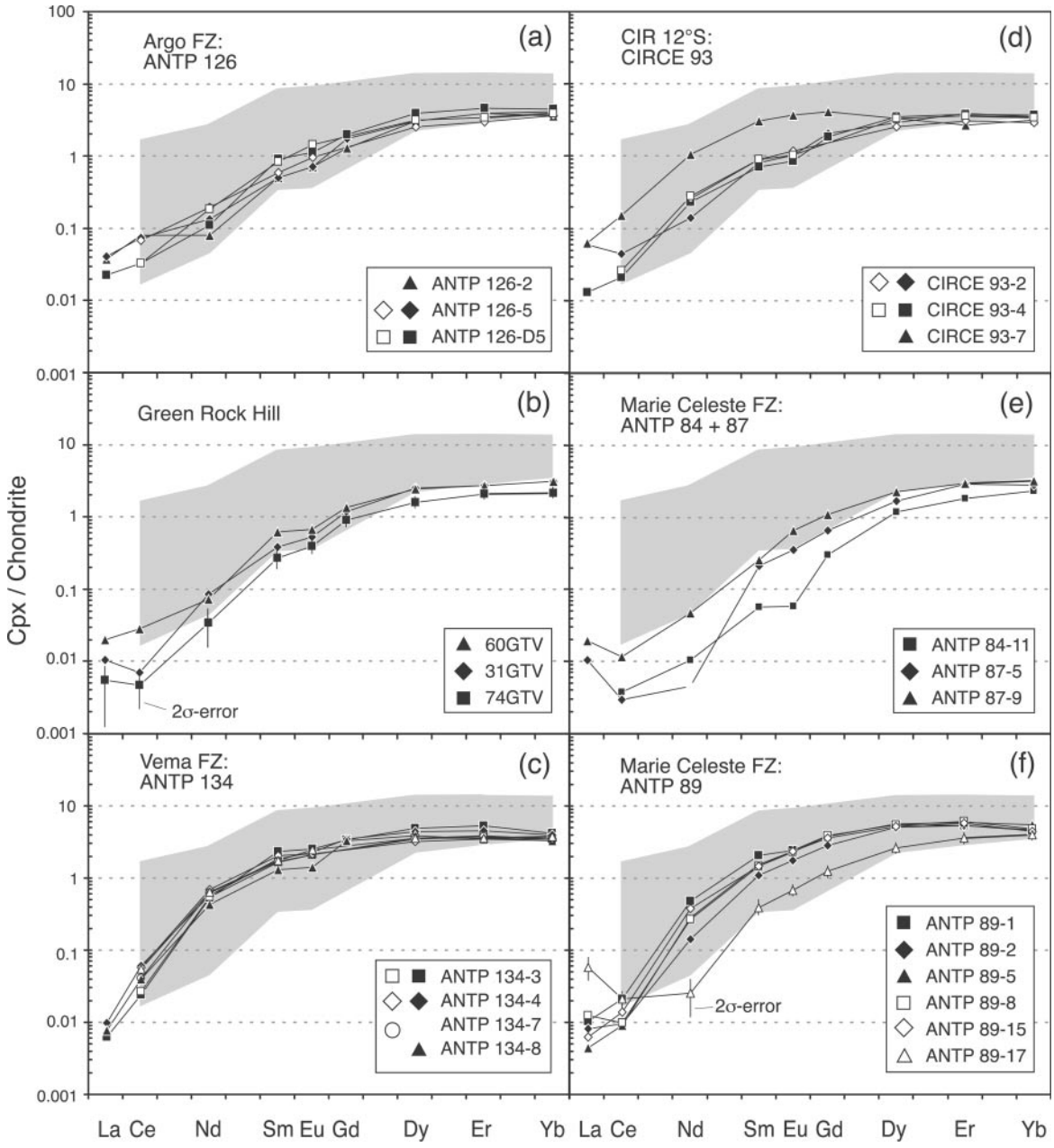

Fig. 5. Chondrite-normalized clinopyroxene rare earth element patterns. Grey field represents the range for abyssal peridotite after Johnson *et al.* (1990). The left panel, (a)–(c), shows cpx REE patterns for Group 1 with hardly any compositional variation. Group 2 samples in the right panel, (d)–(f), have larger within-dredge variation. Filled symbols, MPI analyses; open symbols (except Marie Celeste FZ samples), WHOI analyses. (Further discussion is given in the text.) Typical error (2σ) shown for depleted samples 74GTV and ANTP89-17. CI chondrite normalization values taken from Anders & Grevesse (1989).

samples Vulc5:41-13 and Vulc5:41-15 from the Bullard FZ (Johnson *et al.*, 1990).

Orthopyroxene

Opx shows similar compositional variation to cpx in terms of Mg-number, Al_2O_3 and Cr_2O_3. However, additional geochemical information can be obtained from peridotites in which cpx is absent, or occurs only as fine-grained interstitial grains. In Table 5 only compositions of opx porphyroclast cores are listed. Recrystallized neoblasts have systematically lower Al and Cr content, whereas the Mg-numbers are indistinguishable from porphyroclast compositions. Opx in cpx-free sample

CIRCE93-5 has the lowest Al content (1·76 wt % Al_2O_3) ever reported for mid-ocean ridge melting residues.

Olivine

Olivine compositions could be obtained on only a few samples, because of the strong alteration of the mantle rocks (Table 6). Systematic variations of forsterite (from 0·909 to 0·921) or Ni contents (from 0·37 to 0·40 wt % NiO) with modal or pyroxene composition are not observed. However, the modally depleted harzburgites and dunite from 12°S have the highest forsterite content of all CIR samples.

DISCUSSION

In the following, the generation of cpx trace element patterns by fractional melting will be discussed, either by melting in the stability field of spinel peridotite alone, or by a combination of melting in the garnet peridotite stability field and subsequent further melting under spinel-facies conditions. Finally, processes that disturb simple melting relationships are modelled.

Melting (spinel and garnet stability field)

First, we attempted to match all measured cpx patterns by perfect fractional melting in the spinel stability field. This end-member model simulates immediate removal of every infinitesimal melt increment from the residue, which will rapidly lead to extreme LREE depletions in the residue. Even after a few percent of melt extraction, the La concentration in residual cpx would drop below the detection limit of the ion probe technique. More realistic melting models such as critical melting include finite residual melt porosities (Sobolev & Shimizu, 1992). Because minor amounts of melt (~0·1–1%) are always held back in the residue, the LREE are buffered by this small melt fraction, and their decrease is less drastic. For the MREE to HREE, however, the difference between pure fractional and critical melting is significant only at high melt fractions ($F > \sim 15\%$).

Starting composition and melt modes were identical to those used by Johnson (1998). Several sets of partition coefficients were used. Unless stated otherwise, our mineral–liquid partition coefficients are taken from the compilation of Suhr *et al.* (1998), in which the values are very similar to other such estimates (e.g. Hart & Dunn, 1993; Johnson, 1998). The melting equations used for this modelling are presented in Appendix A, and the starting conditions and partition coefficients used for the modelling are listed in Table 7. The results are shown in Figs 6 and 8 (below).

Spinel peridotite melting with 'normal' D values

Many samples can be modelled by fractional melting of a spinel peridotite starting composition. Group 1 samples in particular have uniform, apparently simple cpx REE patterns. Vema FZ peridotite can be matched well by 10–12% melt extraction in the spinel peridotite stability field using the critical melting equations of Sobolev & Shimizu (1992) with residual melt porosities between 0% (i.e. perfect fractional melting) and 1% (Fig. 6a). The calculated melting curve better reproduces the measured REE pattern at a high (~1%) residual melt porosity, especially for the LREE. Green Rock Hill peridotites can be modelled by 15–17% spinel peridotite melting with similar residual melt porosities (Fig. 6b), although the model cpx do not match all elements. In particular, the observed La and Ce concentrations are too high and require an additional process, which will be discussed below in more detail. Argo FZ samples appear not as depleted as the Green Rock Hill and the Vema FZ samples, because of their relatively high LREE concentrations. Nevertheless, the spinel peridotite melting models shown in Fig. 6c do not match these data. The models always predict far higher MREE concentrations than measured in the sample at the observed HREE concentration ($F \sim 11\%$), or HREE concentrations that are too low at matching MREE ($F \sim 15\%$). A combination of fractional melting followed by batch melting, or vice versa, does not produce matching results either (not shown). Batch melting after fractional melting shifts the cpx REE pattern towards lower absolute concentrations, subparallel to the initial concentration (at the end of fractional melting).

Spinel peridotite melting with compatible HREE

Recent experimental data and theoretical considerations, described by Blundy *et al.* (1998), suggest that HREE are compatible in Na-rich, Al-rich clinopyroxene on the spinel lherzolite solidus at high pressures. According to those workers, this drastically reduces the required involvement of garnet in the MORB melting region. Because of these far-reaching geodynamic implications, we tested their hypothesis from the perspective of the melting residues, and focused on the fractionation between MREE and HREE. Four models simulating melting in the stability field of spinel peridotite were calculated using identical starting conditions but different cpx–liquid partition coefficients. The resulting initial bulk partition coefficients for these models are shown in Fig. 7a. Two melting models use constant partition coefficients: (1) a 'normal' set of $D^{cpx/l}$, adapted from Suhr *et al.* (1998); (2) the Blundy *et al.* (1998) cpx–liquid partition coefficients in which the HREE are moderately compatible in cpx. The two other melting models start with the latter partition coefficients and gradually change to incompatible

Table 7: Melting model: input parameters

	Distribution coefficients*						Source composition†
	ol/l	opx/l	cpx/l (1)	cpx/l (2)	gt/l	sp/l	
La	0·000007	0·0025	0·06	0·09	0·0035	0·0006	0·91
Ce	0·00001	0·005	0·10	0·16	0·008	0·0006	1·4
Nd	0·00007	0·010	0·20	0·36	0·05	0·0006	1·97
Zr	0·004	0·024	0·12	0·27	0·40	0·070	2·18
Sm	0·001	0·020	0·30	0·67	0·22	0·001	2·23
Eu	0·001	0·030	0·37	0·80	0·45	0·001	2·34
Ti	0·015	0·100	0·35	0·71	0·16	0·150	2·46
Dy	0·004	0·050	0·44	1·10	2·0	0·002	2·44
Er	0·009	0·070	0·43	1·44	3·5	0·003	2·46
Yb	0·014	0·090	0·41	1·43	5·0	0·005	2·5

	Source modes‡		Melt modes§	
	Gt-per	Sp-per	Gt-per	Sp-per
olivine	0·57	0·53	0·04	−0·06
opx	0·21	0·27	−0·19	0·28
cpx	0·13	0·17	1·05	0·67
garnet	0·09	0·00	0·11	0·00
spinel	0·00	0·03	0·00	0·11

*From Suhr *et al.* (1998), except cpx/l (2) from Blundy *et al.* (1998).
†From Johnson *et al.* (1990), concentrations normalized to CI chondrite (Anders & Grevesse, 1989).
‡Spinel peridotite modes from Johnson (1998); garnet peridotite modes calculated from sp-peridotite modes using reaction from Johnson *et al.* (1990).
§Garnet peridotite melt modes from Walter (1998); spinel peridotite melt modes from Kinzler (1997).

values with increasing degree of melting. The gradual change from compatible to incompatible HREE in cpx is adapted from Blundy *et al.* (1998) and shown for Yb in Fig. 7b. The only difference between these two 'variable-*D*' models is that one simulates perfect fractional melting and the other critical melting with 0·5% residual melt porosity.

The results are shown in Fig. 8a, plotting the $(Sm/Yb)_N$ ratio (the subscript 'N' denotes that the concentration is normalized to CI chondrite) versus the Yb content of cpx. There is a broad range in measured cpx compositions, but a general trend that with increasing degree of melting both Yb and Sm/Yb decrease. However, at very low Yb concentrations, relatively high Sm/Yb values occur, mainly in the Hess Deep harzburgites. Our main aim is to explain the lowest Sm/Yb at a given (high) Yb concentration, because these provide direct constraints on the melting conditions, rather than on late- or post-melting refertilization (see section 'Coupling and decoupling').

The first fractional melting model that applies the constant incompatible $D^{cpx/l}$ from Suhr *et al.* (1998) shows a rapid decrease in Sm/Yb with decreasing Yb content (Fig. 8a, open circles). However, this pure fractional melting model cannot explain the observed data points that lie below the melting curve. To explain some strongly Sm-depleted samples that still have relatively high Yb concentrations, the melting curve should be steeper. The application of other commonly used 'normal incompatible' $D^{cpx/l}$ (Hart & Dunn, 1993; Johnson, 1998) does not affect this melting trajectory.

The second fractional melting model that uses constant compatible HREE $D^{cpx/l}$ from Blundy *et al.* (1998) is shown only to illustrate extreme, probably unrealistic melting conditions and to provide an upper limit for the variable-*D* models discussed below. It should be noted that the initial clinopyroxene composition is shifted towards a higher Yb concentration with respect to the incompatible-*D* model discussed above, although their initial whole-rock compositions are identical (Fig. 8a,

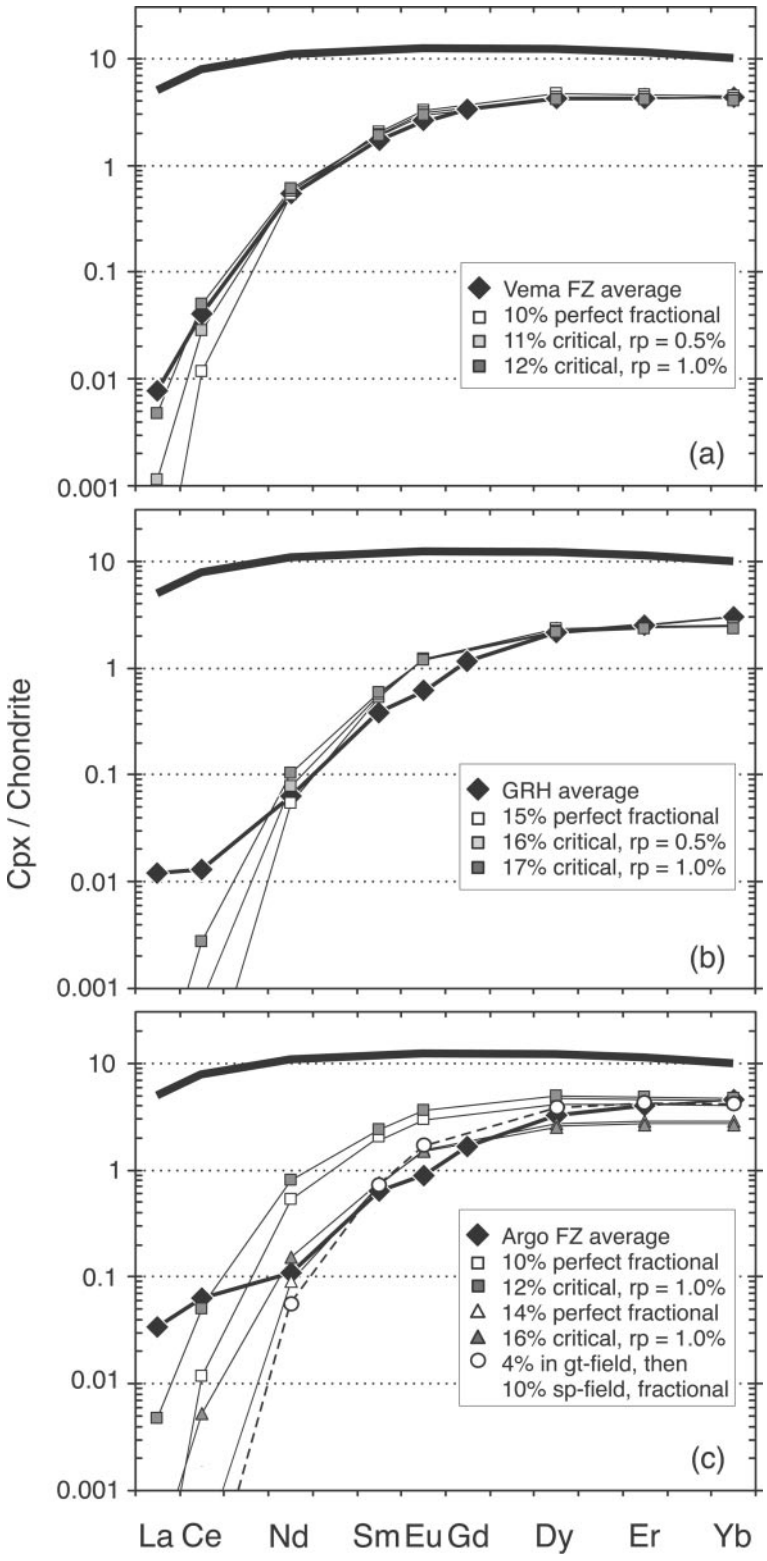

Fig. 6. Result of fractional and critical melting models in the spinel stability field: (a) Vema FZ; (b) Green Rock Hill; (c) Argo FZ. It should be noted that for the Argo cpx, MREE to HREE pattern is too steep to be explained by spinel-field melting alone and requires initial melting of spinel peridotite. Bold black line represents cpx in equilibrium with the depleted mantle source material; rp, residual melt porosity used in the critical melting models.

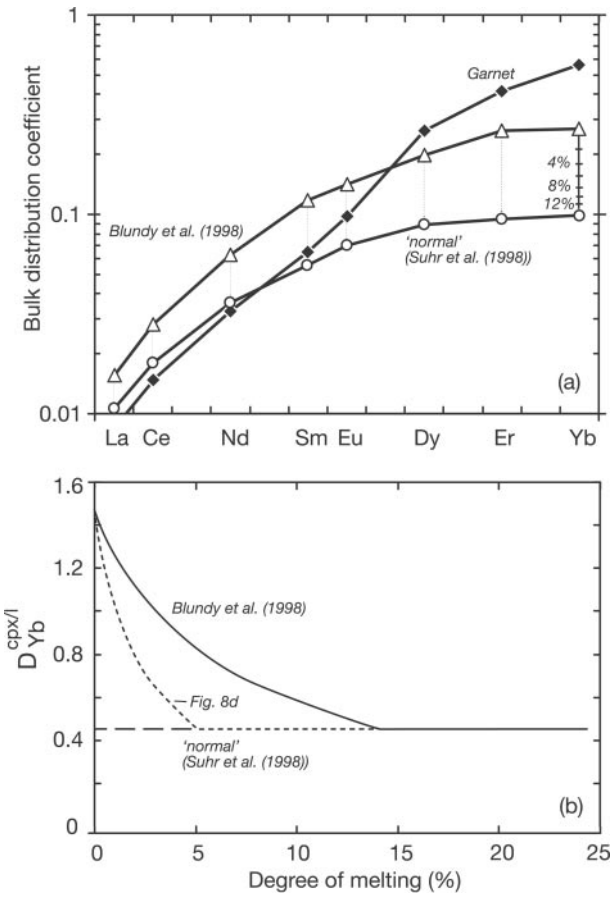

Fig. 7. (a) Initial bulk partition coefficients for the REE used for the spinel peridotite and garnet peridotite melting models. All mineral–liquid partition coefficients were kept constant except $D^{cpx/l}$. ○, 'normal' incompatible $D^{cpx/l}$ (Suhr *et al.*, 1998); △, compatible $D_{HREE}{}^{cpx/l}$ (Blundy *et al.*, 1998); ◆, garnet peridotite using $D^{cpx/l}$ from Suhr *et al.* (1998). (b) Gradual change of $D^{cpx/l}$ for Yb from compatible to incompatible as a function of the degree of melting. Adapted from Blundy *et al.* (1998). Also shown in Fig. 6a by hatch marks for Yb.

closed squares). This model produces a residual cpx with nearly constant Yb as melting progresses. However, $(Sm/Yb)_N$ of the model cpx decreases slowly, especially at very low melt fractions. After 20% melt extraction, both Sm/Yb and Yb are far too high to match the measured cpx compositions. The reason for this non-fractionating behaviour is that Yb is only very moderately compatible and Sm is very moderately incompatible in cpx, both values being close to unity. The more garnet-like behaviour of the HREE in sodic high-pressure cpx by itself is not sufficient to produce a residual clinopyroxenes with fractionated MREE to HREE ratios. The lattice strain model of Blundy & Wood (1994) is able to predict the partitioning behaviour of cpx, commonly graphically expressed by plotting the partition coefficient as a parabolic function of the ionic radius of a given REE. Varying pressure, temperature and composition can tighten or widen the parabola, as well as shift it up and down. However, a real pattern that resembles garnet in which the D values are well below unity for Sm and well above unity for Yb cannot be obtained under any conditions.

Both models that use variable $D^{cpx/l}$ as a function of F as shown in Fig. 7b show a more curved melting trajectory (Fig. 8a). In the first melting increments the residual cpx is similar to the 'constant compatible' case of the second model. After roughly 3% melt extraction, the melting trajectory is subparallel to the first model. The difference between the perfect fractional melting (open triangles) and critical melting with a residual melt porosity of 0·5% (open diamonds) is small and becomes noticeable only at very high degrees of melting. Compared with perfect fractional melting, the cpx in the critical melting model has a composition that is shifted towards slightly higher $(Sm/Yb)_N$ values and Yb concentrations, because the presence of interstitial non-extracted melt has a minor buffering effect on the cpx composition. Overall, these 'variable-$D^{cpx/l}$' models better approach the abyssal peridotite cpx data than the two 'constant-$D^{cpx/l}$' models. However, many clinopyroxenes have $(Sm/Yb)_N$ that are too low at relatively high Yb concentrations to be explained by melting in the stability field of spinel peridotite. This means that a more effective means of depleting MREE with respect to HREE is required to match the observations.

Garnet peridotite melting with 'normal' D *values*

HREE are compatible in garnet, and moderately incompatible in clinopyroxene (Hart & Dunn, 1993; Hauri & Hart, 1995; Johnson, 1998). Variable partition coefficients for garnet can be calculated using strain lattice models similar to those used for clinopyroxene (van Westrenen *et al.*, 1999). For the HREE these do not vary nearly as much as the $D^{cpx/l}$. Spinel cannot accommodate REE in its lattice and therefore does not contribute significantly to the bulk distribution coefficient. Melting in the garnet peridotite field will therefore produce a residue with higher HREE concentrations than melting in the spinel field. This is recorded by the whole-rock MREE/HREE value, which will be much lower after melting in the garnet stability field than in the spinel stability field at the same degree of melt extraction.

Previous workers have asserted that cpx REE patterns of residual abyssal peridotites bear evidence for melting in the stability field of garnet peridotite because of high superchondritic MREE/HREE ratios in certain samples (Johnson *et al.*, 1990). According to those workers residual clinopyroxene develops 'humps' at the MREE to HREE after small amounts of melting of a garnet lherzolite protolith. This is correct as long as the cpx is in equilibrium with residual garnet, because garnet hosts most HREE. After ascent into the stability field of spinel

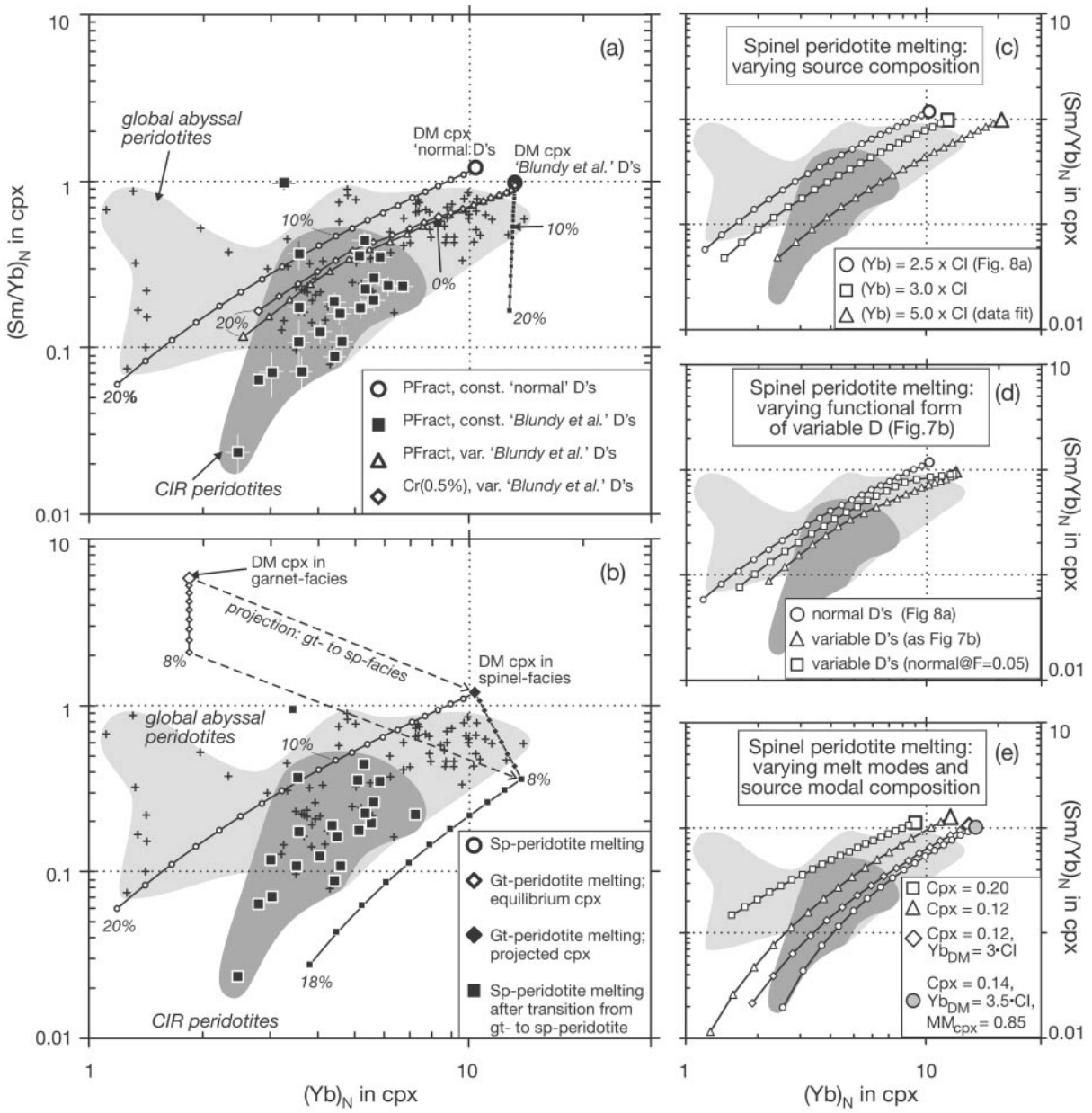

Fig. 8. (a) Yb_N vs $(Sm/Yb)_N$ in clinopyroxenes from the CIR (■) and other abyssal peridotites (+). Curves represent results of perfect fractional (PFract) and critical (Cr) melting models of a spinel peridotite source. The only difference between these models is $D^{cpx/l}$, as shown in Fig. 6. None of these four spinel peridotite melting models can sufficiently explain the low $(Sm/Yb)_N$ ratios at relatively high Yb concentrations in cpx of many residual abyssal peridotites. Input parameters are listed in Table 7. Abyssal peridotite data from Johnson *et al.* (1990), Johnson & Dick (1992), Dick & Natland (1996) and Ross & Elthon (1997). (b) Results of initial garnet peridotite melting followed by subsequent melting in the stability field of spinel peridotite. The strong fractionation of the MREE from the HREE observed in many cpx from abyssal peridotite can only be explained by few percent of initial melting in the garnet stability field before melting in the spinel field. Further discussion is given in the text. (c)–(e) Same diagrams showing results of fractional melting models of spinel peridotite with (c) varying REE concentrations in the DMM source, (d) different functional forms of the gradual change from compatible to incompatible HREE, and (e) source peridotite and melt modes as well as a combination of all. If commonly accepted starting parameters are applied, melting without invoking garnet cannot generate a significant part of the observed values.

peridotite, the garnet-bearing assemblage will react to a garnet-free spinel peridotite. At this garnet breakdown reaction, the REE will be redistributed between the phases of a spinel peridotite assemblage. This will yield an equilibrium cpx with $(Sm/Yb)_N < 1$, rather than a hump-shaped REE pattern. Hump-shaped REE patterns thus cannot be produced by garnet-field melting. Low rather than high MREE to HREE ratios at relatively

high HREE concentrations are the only realistic evidence that the (now garnet-free) spinel peridotites found on the ocean floor preserve information about melting in the presence of residual garnet.

Because cpx REE patterns in a garnet-bearing assemblage can be misleading, we plot cpx REE compositions that are projected from garnet peridotite to spinel peridotite assemblage. This projection simulates cessation of melting in the garnet stability field, followed by an instantaneous breakdown reaction from a garnet to a spinel peridotite assemblage, and it presents the equilibrium cpx composition after ascent into the spinel stability field. This breakdown reaction consumes olivine and garnet and produces two pyroxenes and spinel (Johnson *et al.*, 1990):

$$Mg_2SiO_4\,(Ol) + Ca_{0\cdot75}Mg_{2\cdot25}Al_2Si_3O_{12}(Gt) = 2\cdot5MgSiO_3$$

$$(Opx) + MgAl_2O_4\,(Sp) + 0\cdot75CaMgSi_2O_6\,(Cpx).$$

The projection method reveals that the initial modal compositions for the garnet and spinel peridotite stability field as given by Johnson *et al.* (1990) do not yield an identical starting composition. This is of particular importance, because the initial modal cpx is the most influential and hence crucial parameter of any peridotite melting calculation. Therefore, to model melting in the garnet peridotite field we used the initial spinel peridotite modes (Johnson *et al.*, 1990), which were then recalculated for a spinel-free, garnet-bearing assemblage. All initial modelling parameters are given in Table 7.

In Fig. 8b four fractional melting trajectories are shown. The spinel-facies melting trajectory of Fig. 8a (open circles) using 'normal' incompatible partition coefficients discussed in the previous section is shown for comparison. The garnet peridotite melting trajectory is shown twice: once for actual cpx compositions in equilibrium with garnet (open diamonds) and once for spinel peridotite projected cpx compositions (closed diamonds). This means that cpx in the depleted MORB mantle (DMM) source has an entirely different REE composition depending on whether it coexists with garnet or spinel. In the stability field of garnet peridotite, cpx will have a low Yb concentration and a high Sm/Yb value, because Yb is compatible in the coexisting garnet. Melt extraction will lead to constant Yb concentrations and rapidly decreasing $(Sm/Yb)_N$ in the residual cpx. The garnet stability field melting trajectory that is projected to a garnet-free spinel peridotite assemblage is shifted towards slightly higher Yb concentrations and decreasing Sm/Yb value. A thin dashed line connects a DMM source cpx of real garnet field and projected garnet-free compositions. The latter is identical to a DMM cpx in a spinel peridotite starting material (Fig. 8a). Clearly, $(Sm/Yb)_N$ in cpx decreases more rapidly by garnet field melting than by spinel field melting. Initial garnet field melting followed by spinel field melting is also shown in this diagram, placing an upper boundary on the extent of garnet melting necessary to explain the data. This two-step melting curve can account for any of the observed low $(Sm/Yb)_N$ and the relatively high Yb concentrations for the CIR samples. In contrast to spinel field melting using the partition coefficients from Blundy *et al.* (1998), highly fractionated samples can be explained by reasonable degrees of melting. Major element compositions of some of the very fractionated samples also support moderate degrees of melting. A logical next step would be to repeat the previous melting model, but using variable instead of constant $D^{cpx/l}$. If the results of such a model are plotted in the cpx Yb vs Sm/Yb (not shown), only the projected melting trajectory can be interpreted. Owing to the initially compatible $D^{cpx/l}$, the true garnet field melting trajectory starts at higher Yb and lower Sm/Yb ratios than in the 'constant-D' model. As melting progresses Yb in cpx decreases slowly, at almost constant Sm/Yb. This is solely the effect of the variable $D^{cpx/l}$. The melting curve reflected by the whole-rock composition or the cpx melting path projected to a garnet-free spinel peridotite assemblage is very similar to the 'constant-D' gt-field melting model discussed above. During the garnet-facies steps, the bulk D is still dominated by garnet. After ascent into the spinel field, $D^{cpx/l}$ has already changed to much lower values, having lost its garnet-like behaviour.

For the cpx REE patterns that could not be reproduced by melting in the spinel field alone, a combination of initial melting in the garnet stability field followed by additional melting in the spinel stability field is tested. The Argo FZ samples (ANTP126) can be matched by such a constant-D model. It allows several proportions of melting in the garnet field and subsequent melting in the spinel field. However, a minimum of 3% garnet field fractional melting is required to produce the necessary fractionation between MREE and HREE (Fig. 6c). After this another 9–11% melting in the spinel field is needed to match the measured Argo FZ cpx data. The measured La and Ce concentrations, and to lesser extent Nd, are still too high to be explained by melting and require an additional process, possibly minor amounts of melt entrapment.

All Group 2 samples (CIR axis 12°S, MCFZ) require some melt extraction in the garnet peridotite stability field. Five samples (ANTP89-1, ANTP89-2, ANTP89-5, ANTP89-8 and ANTP89-15) from MCFZ have nearly identical convex-upward LREE-depleted patterns, but cannot be explained by fractional melting in the spinel field alone. Small degrees of melting (3–4%) in the presence of residual garnet, before another 6–8% melting in the spinel field, would match the measurements.

The Sm/Yb value of sample ANTP84-11 can be approached only after high degrees of melting (~6%) in

the garnet peridotite stability field and another ~12% melting during the ascent in the spinel peridotite stability field. Samples ANTP87-5, ANTP87-9 and ANTP89-17 are also extremely depleted, with $(Sm/Yb)_N$ <0·1. These values also require high (~6%) melting in the garnet peridotite stability field followed by ~10% of melting in the spinel stability field. It is not easy to match these results with the relatively low spinel Cr-numbers for these samples (Table 2), which suggest only moderate extents of partial melting. However, chromium is far more compatible under spinel-facies conditions than in a garnet peridotite. Therefore we expect that samples with extensive melting in the garnet field would retain a relatively low spinel Cr-number, as is the case with these four samples.

The hump-shaped REE pattern of CIRCE93-7 (Fig. 5d) cannot at all be explained by melting. Samples CIRCE93-2 and CIRCE93-4 could be the product of 13% critical field melting in the spinel peridotite stability field with residual porosities of 0·5%. The model predicts MREE concentrations that are slightly too high, suggesting that minimal amounts of garnet melting could have occurred before ascent into the spinel peridotite stability field.

In summary, roughly half of the CIR samples cannot be explained by partial melting in the stability field of spinel peridotite but require residual garnet in the source. Up to 8% of melting in the stability field of garnet before melting under spinel peridotite-facies conditions is necessary to reach the strong MREE from HREE fractionation observed in samples from Argo FZ (ANTP126), Marie Celeste FZ (ANTP84, ANTP87, ANTP89), and possibly CIR 12°S (CIRCE93).

Boundary conditions without garnet field melting

It is important to explore how much of the observed Sm/Yb fractionation can be produced without invoking garnet-field melting. A large number of perfect fractional melting models were run with different input parameters, such as source composition, different functional forms to the D_{Yb} vs F relationship (Fig. 7b), melting modes and starting modal composition.

For an alternative estimate of the source composition, we adopted the approach of Shimizu (1998). He proposed a relative abundance pattern of REE, Ti, Zr and Hf for the DMM, which is based on the constraints on Lu–Hf and Sm–Nd systematics developed by Salters & Hart (1989). Ratios of highly incompatible lithophile trace element in unfractionated basalts reflect the source composition, but do not allow a precise estimate of the absolute source concentrations. Therefore we varied the absolute REE concentrations parallel to the pattern derived by Shimizu (1998), for the melting trajectory to fit the data. At an Yb_N of 2·5, this REE pattern is very similar to the starting composition used for the models discussed above, as shown in Fig. 8c. In this way, the melting trajectory can be shifted to higher Yb_N, but the DMM Yb concentration would have to be ~5 times CI chondrite to match the data. This is a factor 1·8–2·5 times higher than all reasonable estimates for the composition of DMM (Hofmann, 1988; Johnson *et al.*, 1990; McDonough & Sun, 1995; Kelemen *et al.*, 1997; Jochum *et al.*, 2000*b*), thus excluding the source composition as the sole cause for our observations.

Blundy *et al.* (1998) proposed that the variable D can be modelled as a function of F. We varied the functional form of this relationship, as depicted in Fig. 7b, the results for a rapid decrease (i.e. D_{HREE} attain normal incompatible values after 5% of melt extraction). The result of this model, as shown in Fig. 8d, suggests that a rapid change from compatible to incompatible D values does not lead to a more efficient fractionation. Given that the compatibility of the HREE in cpx largely depends on the sodium content of cpx, a slower decrease is less likely. Sodium is incompatible in cpx and will be rapidly extracted under fractional melting conditions. Melting with a high melt porosity may buffer the cpx Na content, but will lead to even less fractionation between MREE and HREE.

Further, we varied the modal composition, of both the source peridotite and the melt. The source cpx mode is the most influential parameter of all, and is estimated from systematic modal variations derived by point-counting MAR, CIR, SWIR and AAR peridotites (Dick *et al.*, 1984). As shown in Fig. 8e, a high initial cpx mode of 20% will shift the Sm/Yb vs Yb melting trajectory to the left (open squares), and a lower cpx mode will shift this curve to the right (open triangles). However, applying such a starting mode will lead to early cpx exhaustion, for a initial cpx mode of 12% after 18% of melting. The melt mode is commonly estimated from melting experiments (e.g. Kinzler, 1997; Walter, 1998). One issue is whether these change during melt extraction. Recent experiments have shown that modally depleted peridotites yield the same melting modes as fertile peridotites (Seyler *et al.*, 2001*a*).

Finally, by combining all starting parameters we can generate a melting curve (grey circles in Fig. 8e) that nearly explains the highly fractionated samples and the high Yb samples. The necessary starting conditions must be: (1) a slightly higher cpx melt mode than proposed by Kinzler (1997) (0·85 rather than 0·67), which is not unacceptable, but not supported by experiments either. Further, (2) the initial modal composition must be poorer in cpx than commonly used for modelling melting (~0·14 rather than 0·16). This is similarly plausible. Finally, however, (3) under these conditions the REE budget of the depleted MORB mantle source must be ~40%

higher than commonly accepted (Yb_N at 3·5 rather than 2·5).

These starting conditions were chosen to generate a melting curve that reproduces the extreme data points that cannot be generated by normal, commonly used melting models for trace elements. In the Earth's mantle, these parameters cannot be chosen arbitrarily. Not only is the required REE concentration of the DMM in the last model far higher than any proposed value for DMM (Hofmann, 1988; Johnson *et al.*, 1990; McDonough & Sun, 1995; Kelemen *et al.*, 1997; Jochum *et al.*, 2000*b*), but also the REE content should be coupled to the peridotite cpx mode. Both parameters are exclusively controlled by melt extraction. This is not at all consistent with the requirement of higher initial REE concentrations and a lower cpx modal content. Thus, at least 0–6% melting in the presence of garnet is required for the generation of a large fraction of the global abyssal peridotites, as discussed above. These are minimum values, because perfect fractional melting models were applied.

Coupling and decoupling

Until recently, the decoupling between major and trace elements in residual peridotites was considered a major stumbling block for the understanding of melting and melt migration in the oceanic mantle (e.g. Kelemen *et al.*, 1997). However, major element indicators of melting, such as Cr-number in spinel and Al_2O_3 content in cpx, correlate well with HREE concentrations in cpx of all global abyssal peridotites (Hellebrand *et al.*, 2001). The actual decoupling is confined to the highly incompatible trace elements, which are very poorly or not at all correlated with spinel Cr-number. Therefore, highly incompatible trace elements, such as the LREE, strontium and zirconium, are not well suited for estimating the extent of melting. This does not necessarily mean that the inferences drawn about melting of Johnson *et al.* (1990), which are largely based on the modelling of Ti and Zr, are incorrect. The SWIR and AAR samples for which published cpx trace element and spinel Cr-number are available lie on the expected trend between spinel Cr-number and Zr. It appears that these samples are residual and not strongly affected by late-stage disturbing processes.

With restrictions, however, the highly incompatible trace elements serve as a powerful tool to identify possible late-stage or post-melting processes, such as advective melt percolation, melt entrapment or veining.

Subsolidus veining

Subsolidus veining is probably the least cryptic modification of a residual peridotite. Thin magmatic veinlets that crosscut residual peridotites are widespread and have a dramatic influence on the chemical composition of the phases in a (small) reaction zone surrounding the vein (Cannat *et al.*, 1997; Niida, 1997; Hellebrand *et al.*, 1999). Crosscutting gabbroic dykelets are very common in the exposed MARK area mantle that was drilled during ODP Leg 153. One metre of core contains on average four magmatic veinlets that are mainly <1 cm thick (Cannat *et al.*, 1997). The width of the reaction zone depends on the thickness of the vein. Thick veins produce a chemical gradient that can be easily recognized in the host peridotite. Despite lack of petrographic evidence for subsolidus melt injection in the selected residual CIR samples, a contact zone is probably present in sample ANTP89-2. Here, one spinel grain with an anomalously high Cr-number of 0·49 is present at the edge of the sample. Two other spinels <4 mm away from this anomalous spinel have Cr-number of 0·26. We assume that the sample edge must have been the plane of a very thin crosscutting magmatic veinlet, which produced a reaction zone that is smaller than 4 mm. Because of the intense alteration in this sample, direct evidence for this hypothesis is not available. Observations on other vein-bearing peridotites from the CIR, however, show that the spinel Cr-number strongly increases in a small reaction zone. For five vein-bearing peridotite samples from different locations we obtained detailed major and trace element profiles across the vein phases, the reaction zone and the non-modified host peridotite. In the modified contact zones, primary mineral compositions gradually change from background residual to melt compositions. Variably fractionated melt compositions have been observed; this does not allow us to make a general statement about compositional modifications. The detailed results of this study, and a quantitative model for the interpretation of conditions under which melt injection took place, will be presented elsewhere (Hellebrand *et al.*, in preparation).

Refertilization

A second post-melting modification can be refertilization with a percolating or inefficiently extracted melt that crystallizes on grain boundaries and in interstices. Elthon (1992) noted that cpx of many abyssal peridotites has sodium concentrations that are too high to be residues of fractional melting. He suggested that as melting ceases, residual peridotites are refertilized by a melt that crystallizes and equilibrates with the host peridotite. According to his modelling, the addition of up to 10% depleted basaltic liquid is needed to refertilize a peridotite that previously experienced melt extraction.

In the following, we try to assess the influence of refertilization on the cpx REE composition, irrespective of what the textural implications of such large amounts of trapped melt are. The hump-shaped REE pattern of sample CIRCE93-7 will serve as an extreme case in

which the REE concentrations are dominated by small amounts of trapped melt. As shown in the previous section, the hump-shaped REE pattern of this sample cannot be generated by partial melting, as melt extraction will lead to a strong LREE depletion relative to the HREE. In particular, fractional melting in the stability field of garnet peridotite will produce a residue with very low MREE/HREE values and therefore partial melting in the presence of garnet cannot explain hump-shaped REE patterns in residual clinopyroxenes, as suggested by Johnson *et al.* (1990). The textures of sample CIRCE93-7, as well as the high cpx Na content, suggest that melt extraction was incomplete and led to precipitation of irregular cpx films on olivine–opx grain boundaries (Fig. 2a and b). Coarse clinopyroxenes were not observed in this sample. The very high Mg-numbers of these interstitial cpx are probably not the direct result of very high degrees of melting, but rather of the subsolidus Fe–Mg exchange with olivine.

Quantitative refertilization models require information about the composition of the refertilizing melt, the proportions of the phases that crystallize from it, and the modal and chemical composition of the peridotite before refertilization. The procedure of these calculations is presented in Appendix B.

Intuitively, we expect that a refractory peridotite with very low modal cpx and an (L)REE-depleted cpx composition will respond more dramatically to refertilization than will a fertile cpx-rich lherzolite. This is illustrated by Fig. 9, where $(Sm/Yb)_N$ and $(Ce/Yb)_N$ in cpx are plotted versus Yb_N in cpx for two refertilization models. These models use different peridotite starting modal compositions: a 'depleted' harzburgite with 0·1% modal cpx and a 'fertile' lherzolite with 9% modal cpx. For illustration purposes, both starting modes have identical initial cpx REE concentrations, calculated by 13% critical melting with 0·5% residual melt porosity in the spinel stability field using normal constant partition coefficients and conditions listed in Table 7. In this exercise, the refertilizing agent for both models is a refractory melt, derived from a slightly less depleted peridotite. Its composition represents an instantaneous melt formed at 12% critical melting with 0·5% residual melt porosity (Table 8). After entrapment this melt crystallizes 70% cpx and 30% olivine (Elthon, 1992), after which the newly formed phases equilibrate with the host rock. This crystallization mode does not have a strong effect other than the absolute amount of melt necessary to reproduce the measured pattern, as varying the input parameters has shown. The main controlling parameter on new clinopyroxene chemistry is the composition of the refertilizing melt.

Four important results can be seen immediately from this exercise:

(1) the modally depleted harzburgite is strongly modified by very small amounts of refertilizing melt, whereas the lherzolite responds less dramatically to small amounts of melt added. This is because the REE budget of the lherzolite is buffered by the high initial cpx mode.

(2) The LREE concentration increases much faster than the MREE or even HREE. This is mainly due to the negligible LREE content in the residue before melt entrapment. Large (>1%) amounts of melt are needed to increase the Yb content significantly for both depleted and fertile starting compositions.

(3) Refertilization with a melt that has no hump-shaped REE pattern ($(Sm/Yb)_N < 1$) can produce a clinopyroxene that has a significantly higher $(Sm/Yb)_N$ than the entrapped melt, even at very low amounts of liquid added to the residue. The reason for this non-intuitive behaviour is the important contribution of residual opx to the bulk distribution coefficient. Because of the very high modal abundance of opx relative to cpx in the modally depleted starting material, the largest absolute fraction of the entrapped HREEs will be hosted by opx. Only after modal cpx has exceeded a few percent will the $(Sm/Yb)_N$ in the cpx start to decrease.

(4) Minor amounts of melt added to the residue will produce a dramatic increase of the $(Sm/Yb)_N$ ratio, without modifying the Yb concentration. This could easily obscure the types of garnet stability field melting signature discussed in the previous section, particularly for modally depleted peridotites.

Thus, interstitial melts must be extracted very efficiently, at least from those peridotites that have cpx with $(Sm/Yb)_N$ too low to be explained by spinel peridotite melting. It also means that plagioclase-free peridotites with interstitial (melt-derived) cpx are not residues *senso stricto*, although they may geochemically resemble melting residues. It remains difficult to infer whether very small amounts of melt are trapped in chemically buffered peridotites with more than ~3% modal cpx, especially if these are recrystallized and direct textural information is lost. It is further important to note that melt entrapment does not necessarily lead to plagioclase formation. The chemical 'visibility' of such a melt entrapment strongly depends on the composition of the infiltrating melt and on the modal composition of the residual peridotite.

Chromatographic fractionation

As observed in orogenic lherzolite bodies and mantle sections of ophiolites, simple melt entrapment is not the only process that can modify the composition of a previously depleted peridotite that is devoid of magmatic veins that crosscut the peridotite under subsolidus conditions. Reactive porous flow near a melt transport channel can produce decimetre- to metre-scale zonations and large chemical variations in the melt-infiltrated peridotite (Bodinier *et al.*, 1990; Suhr, 1999). High LREE to HREE ratios are observed at a relatively large distance from

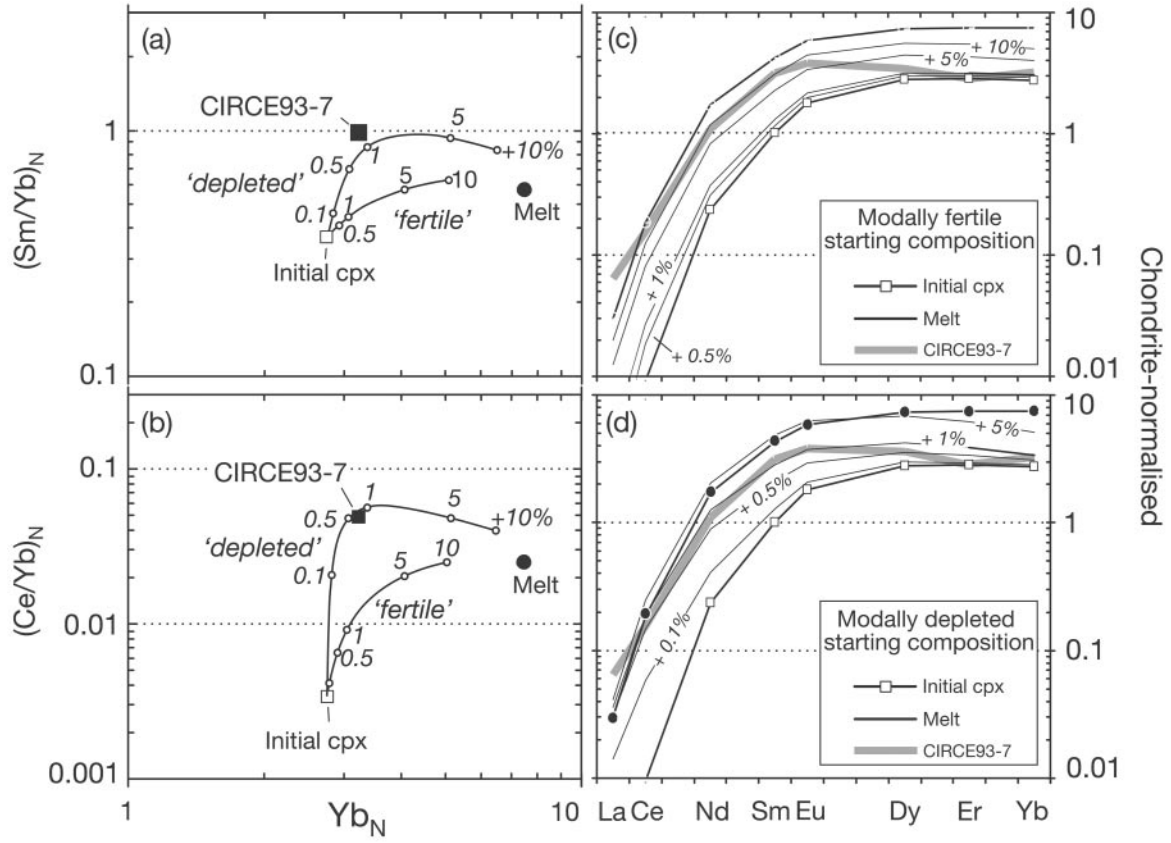

Fig. 9. Results of simple melt entrapment calculations. Mixing and re-equilibration of a modally depleted and a modally fertile residual peridotite with a depleted melt. Starting cpx compositions for the two models are identical. (a) $(Sm/Yb)_N$ and (b) $(Ce/Yb)_N$ vs Yb_N. Refertilization can lead to chondritic $(Sm/Yb)_N$ values in cpx, even if $(Sm/Yb)_N$ in the entrapped melt is subchondritic, resulting from preferential HREE uptake by opx in initially cpx-poor harzburgites. (c) and (d), whole REE patterns for these models using a modally fertile (c) and depleted (d) starting composition.

Table 8: Melt entrapment model: input parameters

	Initial cpx*	Melt†		Initial modes	
				Depleted	Fertile
La	2·2E − 04	0·010	ol	0·85	0·65
Ce	9·2E − 03	0·19	opx	0·139	0·25
Nd	0·235	1·7	cpx	0·001	0·09
Zr	0·118	1·4	sp	0·01	0·01
Sm	1·01	4·3			
Eu	1·80	5·9			
Ti	2·3	7·4			
Dy	2·8	7·3			
Er	2·8	7·5			
Yb	2·8	7·5			

*Calculated residual cpx composition (chondrite normalized) of 13% critical melting with 0·5% residual melt porosity.
†Calculated instantaneous melt composition (chondrite normalized) of 12% critical melting with 0·5% residual melt porosity.

such channels. These enrichments in highly incompatible trace elements are attributed to chromatographic fractionation (Navon & Stolper, 1987). Spoon- or S-shaped REE patterns describing moderate LREE enrichment are also associated with advective melt transport (Godard *et al.*, 2000). Johnson *et al.* (1990) also described four SWIR samples with spoon-shaped patterns attributable to chromatographic processes. Our data suggest that such a process has left its fingerprint in some of the CIR peridotites. Figure 5 shows that six samples have cpx with spoon-shaped REE patterns. Two cpx-poor samples from MCFZ (ANTP87-5, ANTP89-17) show relative enrichments of La and Ce; the other samples (31GTV, 74GTV, CIRCE93-4, ANTP89-8) are only slightly enriched in La. Melting or refertilization calculations fail to explain such patterns, suggesting that chromatographic fractionation may have played a role. Unfortunately, spatial information between individual samples is crucial and detailed geochemical traverses are needed to properly address this problem. Dredged abyssal peridotites are obviously far from ideal for such purposes, but nevertheless valuable to indicate the presence, extent and distribution of reactive melt migration and as a measure of 'ground truth' for the inferences derived from ophiolites and alpine lherzolites.

Small-scale variations

One of the most well-known facts of geochemistry is that the Earth's mantle is isotopically heterogeneous (e.g. Schilling, 1975, 1985; Hofmann, 1997). The scales at which this heterogeneity occurs within the mantle, however, are still a matter of debate. Direct information from oceanic mantle rocks is scarce. Medium-scale (within-dredge) chemical heterogeneity in the 'residual' oceanic mantle has not been given much attention in the literature. Almost all discussions concerned with the origin of abyssal peridotites were restricted to global and regional trends based on local averages, hereby eliminating variations in modal and chemical compositions. Local variations in mineral chemistry occur within a single dredge haul, as noted by Michael & Bonatti (1985), who attributed it partly to subsolidus re-equilibration. Dick *et al.* (1984) also mentioned local heterogeneities, especially for the modal composition, but did not address local chemical variations and they focused their attention on dredge averages.

To address this issue, we divided our sample set into a chemically homogeneous Group 1 and a Group 2 with large chemical heterogeneity on a 'dredge scale'. Some of the Group 2 samples are even heterogeneous on a thin-section scale, as shown by strongly varying spinel Cr-number (Fig. 3). To compare local compositional variation of CIR peridotites with other peridotite occurrences, we selected all dredge hauls for which major and trace element mineral data on three or more samples are available. This yields two dredge hauls from the America–Antarctica Ridge (Bullard FZ and Vulcan FZ) and two from the Southwest Indian Ridge (Bouvet FZ and Islas Orcadas FZ) (Johnson *et al.*, 1990). Further, we selected published Ocean Drilling Program data from Leg 147 at Hess Deep in the Pacific (Dick & Natland, 1996) and from Leg 153 in the MARK area (Ross & Elthon, 1997), where spatial relationships between the individual peridotite samples are known.

Figure 10 shows aluminium, sodium and ytterbium concentrations in cpx versus the Cr-number of the associated spinel for all selected samples. Drilled residual peridotites have almost constant major and trace element compositions throughout the boreholes. Four out of nine dredge hauls are compositionally relatively homogeneous, although there is more variation than in the boreholes. Three dredges (Vulcan FZ, Islas Orcadas FZ, Vema FZ) show substantial chemical variation, especially for sodium. The peridotites from CIR 12°S and Marie Celeste FZ are very heterogeneous.

The causes for local heterogeneities remain largely enigmatic. However, our observations may serve as a guide for future studies with respect to some aspects: (1) inefficient melt extraction, as seen in the Vema FZ harzburgites, does not necessarily lead to heterogeneity; (2) reactive porous melt flow in and near dunitic channels can produce large chemical gradients and modal heterogeneity on an outcrop scale, as is observed in the mantle sections of ophiolites (Kelemen *et al.*, 1992; Suhr, 1999). The extremely depleted modal and chemical composition of Hess Deep harzburgites can also be attributed to this process (Dick & Natland, 1996). In contrast to the very heterogeneous CIR 12°S peridotites, which bear evidence for melt–rock reaction, Hess Deep peridotites are relatively homogeneous. Possibly, the melt supply is more continuous beneath the fast-spreading EPR than beneath the intermediate-spreading CIR.

CONCLUSIONS

(1) Clinopyroxenes in plagioclase- and vein-free abyssal peridotites from the intermediate-spreading Central Indian Ridge are generally more depleted in incompatible trace element than those in similar peridotites from the slower-spreading Southwest Indian and America–Antarctica ridges.

(2) Although the general features of the cpx REE patterns can be modelled by perfect fractional melting in the spinel stability field, roughly half of the CIR melting residues require initial melting (up to 6%) in the presence of garnet. Garnet in the melting region is necessary to explain the low MREE to HREE ratios. Recently published cpx partition coefficients (Blundy *et*

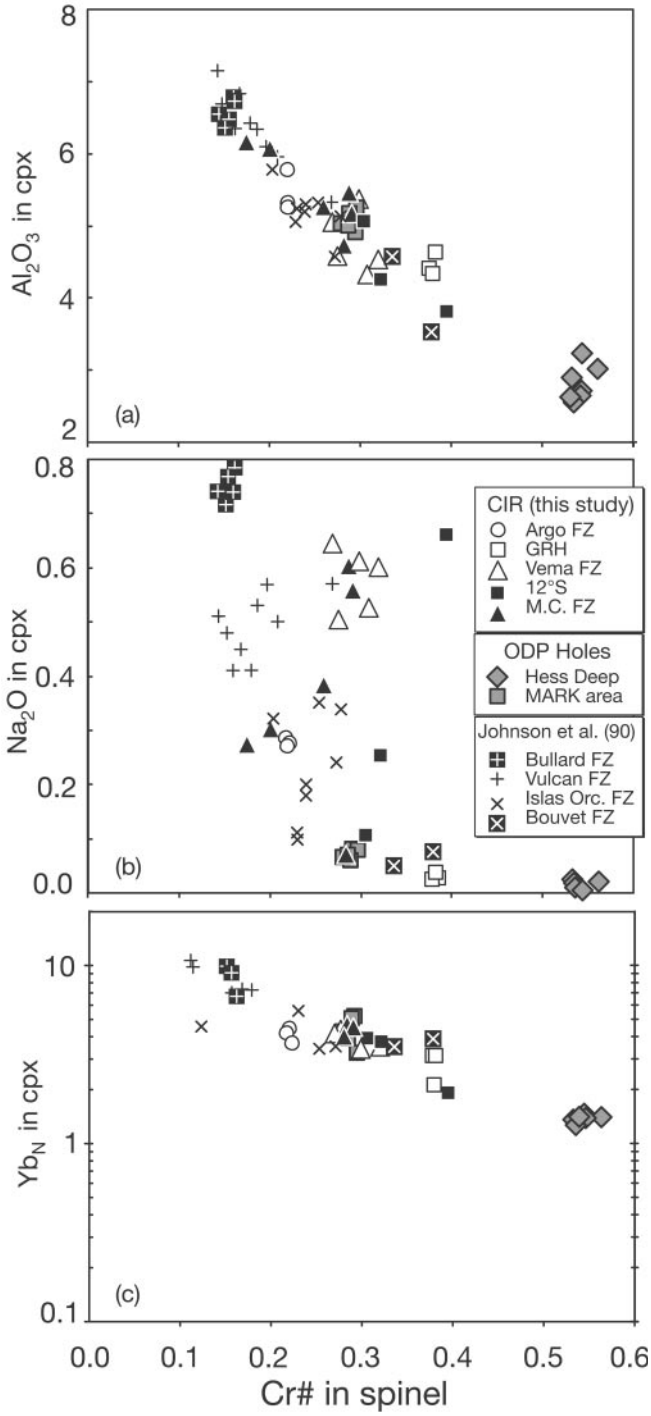

Fig. 10. (a) Al_2O_3, (b) Na_2O and (c) Yb_N in cpx vs Cr-number in associated spinel. Large variations in mineral chemistry on a local scale (dredge haul, borehole) have been observed at some locations but appear to be absent at others. Further study of residual abyssal peridotites is required to address the scales, extent and causes of chemical heterogeneity in the Earth's mantle.

al., 1998), which suggest that HREE are compatible in cpx at high pressures, are believed to mimic the garnet signature of many MORB glasses. Fractional and critical melting models that apply these new $D^{cpx/l}$ fail to explain the low Sm/Yb values in cpx of many CIR and other abyssal peridotites.

(3) Textures of the Central Indian Ridge peridotites indicate that efficiency of melt extraction is variable. At

olivine–olivine and olivine–opx grain boundaries of some samples, melt-derived interstitial cpx crystallized. The cpx trace element signature of modally and chemically depleted melting residues is highly susceptible to minor (<1%) amounts of trapped melt. However, 'trapped melt' is not reflected automatically by the mineral chemistry; it largely depends on the modal cpx content that was present before melt entrapment and the chemistry of the refertilizing melt.

(4) 'Hump-shaped' REE patterns cannot be generated by melting in the garnet field as asserted by Johnson *et al.* (1990). They can be produced by the refertilization with a depleted melt as a result of the leverage of opx on the bulk distribution coefficient.

(5) The chemical composition of relict mantle phases in the CIR peridotite varies strongly in some dredge hauls and is constant in others. A comparison with the two available oceanic mantle boreholes reveals that the mantle away from crosscutting dykelets has very limited compositional variation. Apparently, parts of the CIR are more heterogeneous on a small to medium scale. In such areas of large local variations, exact spatial information between individual samples can be provided by other recovery methods, such as drilling. These are required to address the causes, extent and scales of heterogeneities in the oceanic mantle, and whether they are preserved or produced by melting or melt migration.

ACKNOWLEDGEMENTS

E.H. is indebted to Nobu Shimizu and Graham Layne for their help on the WHOI ion probe, and to Astrid Besmehn and Elmar Groener on the Mainz ion probe. We thank Beate Mocek and Günter Suhr for informal reviews. Constructive reviews by Kevin Johnson, Tim Elliott and Jon Blundy greatly improved this paper.

REFERENCES

Anders, E. & Grevesse, N. (1989). Abundances of the elements: meteoric and solar. *Geochimica et Cosmochimica Acta* **53**, 197–214.

Asimow, P. D. (1999). A model that reconciles major- and trace-element data from abyssal peridotites. *Earth and Planetary Science Letters* **169**, 303–319.

Aumento, F. & Loubat, H. (1971). The Mid-Atlantic Ridge near 45°N. Serpentinized ultramafic intrusions. *Canadian Journal of Earth Sciences* **8**, 631–663.

Baxter, A. N., Upton, B. & White, W. M. (1985). Petrology and geochemistry of Rodrigues Island, Indian Ocean. *Contributions to Mineralogy and Petrology* **89**, 90–101.

Beattie, P. (1993). Uranium–thorium disequilibria and partitioning on melting of garnet peridotite. *Nature* **363**, 63–65.

Blundy, J. & Wood, B. (1994). Prediction of crystal–melt partition coefficients from elastic moduli. *Nature* **372**, 452–454.

Blundy, J., Robinson, J. A. C. & Wood, B. (1998). Heavy REE are compatible in clinopyroxene on the spinel lherzolite solidus. *Earth and Planetary Science Letters* **160**, 493–504.

Bodinier, J. L., Vasseur, G., Vernières, J., Dupuy, C. & Fabriès, J. (1990). Mechanisms of mantle metasomatism: geochemical evidence from the Lherz orogenic peridotite. *Journal of Petrology* **31**, 597–628.

Bottinga, Y. & Allègre, C. J. (1978). Partial melting under spreading ridges. *Philosophical Transactions of the Royal Society of London, Series A* **288**, 501–525.

Bourdon, B., Langmuir, C. H., Elliott, T. & Zindler, A. (1996). Constraints on mantle melting at mid-ocean ridges from global ^{238}U–^{230}Th disequilibrium data. *Nature* **384**, 231–235.

Briais, A. (1995). Structural analysis of the segmentation of the Central Indian Ridge between 20°30′S and 25°30′S (Rodriguez Triple Junction). *Marine Geophysical Researches* **17**, 431–467.

Cannat, M. (1993). Emplacement of mantle rocks in the seafloor at mid-ocean ridges. *Journal of Geophysical Research* **98**, 4163–4172.

Cannat, M., Chatin, F., Whitechurch, H. & Ceuleneer, G. (1997). Gabbroic rocks trapped in the upper mantle at the Mid-Atlantic Ridge. In: Karson, J. A., Cannat, M., Miller, D.J., *et al.* (eds) *Proceedings of the Ocean Drilling Program, Scientific Results, 153*. College Station, TX: Ocean Drilling Program, pp. 243–264.

Debayle, E. & Leveque, J. J. (1997). Upper mantle heterogeneities in the Indian Ocean from waveform inversions. *Geophysical Research Letters* **24**, 245–248.

DeMets, C., Gordon, R. G., Argus, D. F. & Stein, S. (1990). Current plate motions. *Geophysical Journal International* **101**, 425–478.

Dick, H. J. B. (1989). Abyssal peridotites, very slow spreading ridges and ocean ridge magmatism. In: Saunders, A. D. & Norry, M. J. (eds) *Magmatism in the Ocean Basins. Geological Society, London, Special Publications* **42**, 71–105.

Dick, H. J. B. & Bullen, T. (1984). Chromian spinel as a petrogenetic indicator in abyssal and alpine-type peridotites and spatially associated lavas. *Contributions to Mineralogy and Petrology* **86**, 54–76.

Dick, H. J. B. & Natland, J. H. (1996). Late-stage melt evolution and transport in the shallow mantle beneath the East Pacific Rise. In: Mével, C., Gillis, K. M., Allan, J.F., *et al.* (eds) *Proceedings of the Ocean Drilling Program, Scientific Results, 147*. College Station, TX: Ocean Drilling Program, pp. 103–134.

Dick, H. J. B., Fisher, R. L. & Bryan, W. B. (1984). Mineralogic variability of the uppermost mantle along mid-ocean ridges. *Earth and Planetary Science Letters* **69**, 88–106.

Dupré, B. & Allègre, C. J. (1983). Pb–Sr isotope variation in Indian Ocean basalts and mixing phenomena. *Nature* **303**, 142–146.

Dyment, J. (1998). Evolution of the Carlsberg Ridge between 60 and 45 Ma: ridge propagation, spreading asymmetry, and the Deccan–Reunion hotspot. *Journal of Geophysical Research* **103**, 24067–24084.

Elthon, D. (1992). Chemical trends in abyssal peridotites; refertilization of depleted suboceanic mantle. *Journal of Geophysical Research* **97**, 9015–9025.

Engel, C. G. & Fisher, R. L. (1975). Granitic to ultramafic rock complexes of the Indian Ocean ridge system, western Indian Ocean. *Geological Society of America Bulletin* **24**, 1553–1578.

Gaetani, G. A. & Grove, T. L. (1995). Partitioning of rare earth elements between clinopyroxene and silicate melt: crystal-chemical controls. *Geochimica et Cosmochimica Acta* **59**, 1951–1962.

Gallahan, W. E. & Nielsen, R. L. (1992). The partitioning of Sc, Y, and the rare earth elements between high-Ca pyroxene and natural mafic to intermediate lavas at 1-atmosphere. *Geochimica et Cosmochimica Acta* **56**, 2387–2404.

Gast, P. W. (1968). Trace element fractionation and the origin of tholeiitic and alkalic magma types. *Geochimica et Cosmochimica Acta* **32**, 1057–1086.

Godard, M., Jousselin, D. & Bodinier, J. L. (2000). Relationships between geochemistry and structure beneath a palaeo-spreading centre: a study of the mantle section in the Oman ophiolite. *Earth and Planetary Science Letters* **180**, 133–148.

Green, D. H. & Ringwood, A. E. (1967). The genesis of basaltic magmas. *Contributions to Mineralogy and Petrology* **15**, 103–190.

Green, D. H. & Ringwood, A. E. (1970). Mineralogy of peridotitic compositions under upper mantle conditions. *Physics of the Earth and Planetary Interiors* **3**, 359–371.

Hamlyn, P. R. & Bonatti, E. (1980). Petrology of mantle-derived ultramafics from the Owen Fracture Zone, Northwest Indian Ocean: implications for the nature of the oceanic upper mantle. *Earth and Planetary Science Letters* **48**, 65–79.

Hart, S. R. (1984). A large-scale isotope anomaly in the southern-hemisphere mantle. *Nature* **309**, 753–757.

Hart, S. R. & Dunn, T. (1993). Experimental cpx/melt partitioning of 24 elements. *Contributions to Mineralogy and Petrology* **113**, 1–18.

Hauri, E. & Hart, S. (1995). Corrections to "Constraints on melt migration from mantle plumes; a trace element study of peridotite xenoliths from Savai'i, western Samoa". *Journal of Geophysical Research* **100**, 2003.

Hellebrand, E., Snow, J. E., Dick, H. J. B., Devey, C. W. & Hofmann, A. W. (1999). Reactive crack flow in the oceanic mantle: an ion probe study on cpx from vein-bearing abyssal peridotites. *Ofioliti* **24**, 106–107.

Hellebrand, E., Snow, J. E., Dick, H. J. B. & Hofmann, A. W. (2001). Coupled major and trace elements as indicators of the extent of melting in mid-ocean-ridge peridotites. *Nature* **410**, 677–681.

Hofmann, A. W. (1988). Chemical differentiation of the Earth; the relationship between mantle, continental crust, and oceanic crust. *Earth and Planetary Science Letters* **90**, 297–314.

Hofmann, A. W. (1997). Mantle geochemistry: the message from oceanic volcanism. *Nature* **385**, 219–229.

Irving, A. J. & Frey, F. A. (1978). Distribution of trace elements between garnet megacrysts and host volcanic liquids of kimberlitic to rhyolitic composition. *Geochimica et Cosmochimica Acta* **42**, 771–787.

Jochum, K. P., Dingwell, D. B., Rocholl, A., Stoll, B., Hofmann, A. W., Becker, S., *et al.* (2000*a*). The preparation and preliminary characterisation of eight geological MPI-DING standard reference glasses for in-situ microanalysis. *Geostandards Newsletter* **24**, 87–133.

Jochum, K. P., Stolz, A. J. & McOrist, G. (2000*b*). Niobium and tantalum in carbonaceous chondrites: constraints on the solar system and primitive mantle niobium/tantalum, zirconium/niobium, and niobium/uranium ratios. *Meteoritics and Planetary Science* **35**, 229–235.

Johnson, K. T. M. (1998). Experimental determination of partition coefficients for rare earth and high-field-strength elements between clinopyroxene, garnet, and basaltic melt at high pressures. *Contributions to Mineralogy and Petrology* **133**, 60–68.

Johnson, K. T. M. & Dick, H. J. B. (1992). Open system melting and temporal and spatial variation of peridotite and basalt at the Atlantis II fracture zone. *Journal of Geophysical Research* **97**, 9219–9241.

Johnson, K. T. M., Dick, H. J. B. & Shimizu, N. (1990). Melting in the oceanic upper mantle; an ion microprobe study of diopsides in abyssal peridotites. *Journal of Geophysical Research* **95**, 2661–2678.

Kelemen, P. B., Dick, H. J. B. & Quick, J. E. (1992). Formation of harzburgite by pervasive melt/rock reaction in the upper mantle. *Nature* **358**, 635–641.

Kelemen, P. B., Hirth, G., Shimizu, N., Spiegelman, M. & Dick, H. J. B. (1997). A review of melt migration processes in the adiabatically upwelling mantle beneath oceanic spreading ridges. *Philosophical Transactions of the Royal Society of London* **355**, 283–318.

Kinzler, R. J. (1997). Melting of mantle peridotite at pressures approaching the spinel to garnet transition: application to mid-ocean ridge basalt petrogenesis. *Journal of Geophysical Research* **102**, 953–974.

Klein, E. M. & Langmuir, C. H. (1987). Global correlations of ocean ridge basalts with axial depth and crustal thickness. *Journal of Geophysical Research* **92**, 8089–8115.

Langmuir, C. H., Klein, E. M. & Plank, T. (1992). Petrologic systematics of mid-ocean ridge basalts: constraints on melt generation beneath ocean ridges. In: Phipps-Morgan, J., Blackman, D. K. & Sinton, J. M. (eds) *Mantle Flow and Melt Generation at Mid-Ocean Ridges. Geophysical Monograph, American Geophysical Union* **71**, 183–280.

LaTourette, T. Z., Kennedy, A. K. & Wasserburg, G. J. (1993). Thorium–uranium fractionation by garnet: evidence for a deep source and rapid rise of oceanic basalts. *Science* **261**, 739–742.

Lundstrom, C. C., Shaw, H. F., Ryerson, F. J., Phinney, D. L., Gill, J. & Williams, Q. (1994). Compositional controls on the partitioning of U, Th, Ba, Pb, Sr and Zr between clinopyroxene and hyplobasaltic melts—implications for uranium series disequilibria in basalts. *Earth and Planetary Science Letters* **128**, 407–423.

Lundstrom, C. C., Gill, J., Williams, Q. & Perfit, M. (1995). Mantle melting and basalt extraction by equilibrium porous flow. *Science* **270**, 1958–1961.

Lundstrom, C. C., Gill, J. & Williams, Q. (2000). A geochemically consistent hypothesis for MORB generation. *Chemical Geology* **162**, 105–126.

Maaloe, S. (1982). Geochemical aspects of permeability controlled partial melting and fractional crystallization. *Geochimica et Cosmochimica Acta* **46**, 43–57.

Mahoney, J. J. (1988). Deccan traps. In: MacDougall, J. D. (ed.) *Continental Flood Basalts*. Dordrecht: Kluwer Academic, pp. 151–194.

Mahoney, J. J., Natland, J. H., White, W. M., Poreda, R., Bloomer, S. H., Fisher, R. L. & Baxter, A. N. (1989). Isotopic and geochemical provinces of the Western Indian Ocean spreading centers. *Journal of Geophysical Research* **94**, 4033–4052.

McDonough, W. F. & Sun, S.-S. (1995). The composition of the Earth. *Chemical Geology* **120**, 223–253.

McDougall, I. & Chamalaun, F. G. (1969). Isotopic dating and geomagnetic polarity studies on volcanic rocks from Mauritius, Indian Ocean. *Geological Society of America Bulletin* **80**, 1419–1442.

McKenzie, D. (1984). The generation and compaction of partially molten rock. *Journal of Petrology* **25**, 713–765.

McKenzie, D. & Bickle, M. J. (1988). The volume and composition of melt generated by extension of the lithosphere. *Journal of Petrology* **29**, 625–679.

Mercier, J. C. & Nicolas, A. (1975). Textures and fabrics of upper-mantle peridotites as illustrated by xenoliths from basalts. *Journal of Petrology* **16**, 454–487.

Michael, P. J. & Bonatti, E. (1985). Peridotite composition from the North Atlantic; regional and tectonic variations and implications for partial melting. *Earth and Planetary Science Letters* **73**, 91–104.

Morgan, W. J. (1978). Rodriguez, Darwin, Amsterdam, . . . , a second type of hotspot island. *Journal of Geophysical Research* **83**, 5355–5360.

Natland, J. (1991). Indian Ocean crust. In: Floyd, P. A. (ed.) *Oceanic Basalts*. Glasgow: Blackie, pp. 289–310.

Navon, O. & Stolper, E. (1987). Geochemical consequences of melt percolation: the upper mantle as a chromatographic column. *Journal of Geology* **95**, 285–307.

Niida, K. (1997). Mineralogy of MARK peridotites: replacement through magma channeling examined from Hole 920D, MARK area. In: Karson, J. A., Cannat, M., Miller, D. J. *et al.* (eds) *Proceedings of the Ocean Drilling Program, Scientific Results, 153*. College Station, TX: Ocean Drilling Program, pp. 243–264.

O'Hara, M. J. (1985). Importance of the shape of the melting regime during partial melting of the mantle. *Nature* **314**, 58–62.

O'Hara, M. J., Richardson, S. W. & Wilson, G. (1971). Garnet-peridotite stability and occurrence in crust and mantle. *Contributions to Mineralogy and Petrology* **32**, 48–68.

Rehkämper, M. & Hofmann, A. W. (1997). Recycled ocean crust and sediment in Indian Ocean MORB. *Earth and Planetary Science Letters* **147**, 93–106.

Ross, K. & Elthon, D. (1997). Extreme incompatible trace-element depletion of diopside in residual mantle from south of the Kane F.Z. In: Karson, J. A., Cannat, M., Miller, D. J. *et al.* (eds) *Proceedings of the Ocean Drilling Program, Scientific Results, 153*. College Station, TX: Ocean Drilling Program, pp. 277–284.

Salters, V. J. M. (1996). The generation of mid-ocean ridge basalts from the Hf and Nd isotope perspective. *Earth and Planetary Science Letters* **141**, 109–123.

Salters, V. J. M. & Hart, S. R. (1989). The hafnium paradox and the role of garnet in the source of mid-ocean ridge basalts. *Nature* **342**, 420–422.

Schiano, P., Birck, J. L. & Allègre, C. A. (1997). Osmium–strontium–neodymium–lead isotopic covariations in mid-ocean ridge glasses and the heterogeneity of the upper mantle. *Earth and Planetary Science Letters* **150**, 363–379.

Schilling, J.-G. (1975). Azores mantle blob: rare earth evidence. *Earth and Planetary Science Letters* **25**, 103–115.

Schilling, J.-G. (1985). Upper mantle heterogeneities and dynamics. *Nature* **314**, 62–67.

Seyler, M., Toplis, M. J., Laporte, D. & Ratteron, P. (2001*a*). Experimental determination of melting reactions and liquid compositions produced by small degree melting of depleted peridotite. *Journal of Conference Abstracts* **6**, 450.

Seyler, M., Toplis, M. J., Lorand, J.-P., Luguet, A. & Cannat, M. (2001*b*). Clinopyroxene microtextures reveal incompletely extracted melt in abyssal peridotites. *Geology* **29**, 155–158.

Shaw, D. M. (1970). Trace element fractionation during anatexis. *Geochimica et Cosmochimica Acta* **34**, 237–243.

Shen, Y. & Forsyth, D. W. (1995). Geochemical constraint on initial and final depths of melting beneath mid-ocean ridges. *Journal of Geophysical Research* **100**, 2211–2237.

Shimizu, N. (1998). The geochemistry of olivine-hosted melt inclusions in a FAMOUS basalt ALV519-4-1. *Physics of the Earth and Planetary Interiors* **107**, 183–201.

Shimizu, N., Semet, M. P. & Allègre, J. C. (1978). Geochemical applications of quantitative ion microprobe analysis. *Geochimica et Cosmochimica Acta* **42**, 1321–1334.

Sinton, J. (1978). Petrology of (alpine-type) peridotites from Site 395, DSDP Leg 45. In: Melson, W. G., Rabinowitz, P. D. *et al.* (eds) *Initial Reports of the Deep Sea Drilling Project, 45*. Washington, DC: US Government Printing Office, pp. 595–601.

Sobolev, A. V. (1996). Melt inclusions in minerals as a source of principle petrological information. *Petrology* **4**, 209–220.

Sobolev, A. V. & Shimizu, N. (1992). Extremely depleted magmas and oceanic mantle permeability. *Doklady Rossiyskoy Akademii Nauk* **326**, 354–360.

Spiegelman, M. & Elliott, T. (1993). Consequences of melt transport for uranium series disequilibrium. *Earth and Planetary Science Letters* **118**, 1–20.

Suhr, G. (1999). Melt migration under oceanic ridges: inferences from reactive transport modelling of upper mantle hosted dunites. *Journal of Petrology* **40**, 575–599.

Suhr, G., Seck, H. A., Shimizu, N., Günther, D. & Jenner, G. (1998). Infiltration of refractory melts into the lowermost oceanic crust: evidence from dunite- and gabbro-hosted clinopyroxenes in the Bay of Islands Ophiolite. *Contributions to Mineralogy and Petrology* **131**, 136–154.

Takahashi, E. (1986). Melting of a dry peridotite KLB-1 up to 14 GPa: implications on the origin of peridotitic upper mantle. *Journal of Geophysical Research* **91**, 9367–9382.

Tartarotti, P., Cannat, M. & Mevel, C. (1995). Gabbroic dikelets in serpentinized peridotites from the Mid-Atlantic Ridge at 23°20′N. In: Vissers, R. & Nicolas, A. (eds) *Mantle and Lower Crust Exposed in Oceanic Ridges and in Ophiolites*. Dordrecht: Kluwer Academic, 214-2 pp.

van Westrenen, W., Blundy, J. & Wood, B. (1999). Crystal-chemical controls on trace element partitioning between garnet and anhydrous silicate melt. *American Mineralogist* **84**, 838–847.

Walter, M., J. (1998). Melting of garnet peridotite and the origin of komatiite and depleted lithosphere. *Journal of Petrology* **39**, 29–60.

Wood, B. J. & Blundy, J. D. (1997). A predictive model for rare earth element partitioning between clinopyroxene and anhydrous silicate melt. *Contributions to Mineralogy and Petrology* **129**, 166–181.

Zinner, E. & Crozaz, C. (1986). A method for the quantitative measurement of rare earth elements in the ion probe. *International Journal of Mass Spectrometry and Ion Processes* **69**, 17–38.

APPENDIX A

Perfect non-modal fractional melting was calculated using the general equations derived by Gast (1968) and Johnson *et al.* (1990). The concentration of element i in the peridotite residue, C_{wr}, at melt fraction F is

$$C_{wr} = \left(\frac{C_0}{1-F}\right)\left(1-\frac{PF}{D_0}\right)^{1/P} \quad \text{(A1)}$$

where C_0 is the initial whole-rock concentration. The initial bulk distribution coefficient D_0 is defined as

$$D_0 = \Sigma(Kd_i^{j/1}M_{0j}) \quad \text{(A2)}$$

where M_{0j} is the initial mineral mode of phase j, and $D_j^{j/1}$ is the experimentally determined mineral–liquid partition coefficient of phase j. Similarly, as melting is non-modal, the melt mode P describes the phase proportions that enter the melt:

$$P = \Sigma(Kd^{j/1}p_j) \quad \text{(A3)}$$

where p_j is the melt mode of phase j. The melt modes for garnet and spinel stability field are taken from Walter (1998) and Kinzler (1997), respectively. A residual clinopyroxene that is in equilibrium with the whole rock has a trace element concentration

$$C_{cpx} = \frac{Kd^{cpx/1}}{D_{bulk}}C_{wr} \quad \text{(A4)}$$

which can be rewritten as

$$C_{cpx} = \frac{Kd^{cpx/1}C_0}{D_{bulk}(1-F)}\left(1-\frac{PF}{D_0}\right)^{1/P}. \quad \text{(A5)}$$

The bulk distribution coefficient, D_{bulk}, changes during partial melting, because the mineral modes M_j change as a function of melt fraction F:

$$D_{\text{bulk}} = \Sigma(Kd^{j/1}M_j) \tag{A6}$$

and

$$M_j = M_{0,j}(1-X) + Xp_j. \tag{A7}$$

Critical melting (Maaloe, 1982) is a more sophisticated melting model, which accounts for a small residual melt porosity α. The rationale behind this melt porosity is that 'critical' melt fractions cannot be segregated perfectly from the peridotite, but are retained on the grain boundaries or in interstices. At melt fractions below the residual melt porosity, the system is closed and compositions of melt and residue can be described by batch (equilibrium) melting equations (Shaw, 1970). Only when the melt fraction exceeds the residual melt porosity is a melt fraction of $(F - \alpha)$ extracted from the residual solid and the residual interstitial melt. The melt phase retained in these pores buffers the LREE budget of the residue at high melt fractions. The exact solution has been described for the liquid composition in two steps by Sobolev & Shimizu (1992). The solid residue can be described as follows: for $0 \leq F < \alpha/(\alpha + 1)$

$$C_{\text{wr}} = \left(\frac{D_0 - PF}{1-F}\right)\left[\frac{C_0}{D_0 + F(1-P)}\right] \tag{A8}$$

and for $F \geq \alpha/(\alpha + 1)$

$$C_{\text{wr}} = \left(\frac{D_0 - DF}{1-F}\right)\left[\frac{C_0}{D_0 + (1-P).\dfrac{\alpha}{\alpha+1}}\right] \left[\frac{(D_0+\alpha)-(P+\alpha)F}{(D_0+\alpha)-(P+\alpha).\dfrac{\alpha}{\alpha+1}}\right]^{(1-P)/(P+\alpha)}. \tag{A9}$$

These equations for critical melting were solved numerically applying the CMELT program developed by G. Suhr.

APPENDIX B

The chemical effect of melt entrapment on a residual peridotite is derived in four simple steps. First, the new whole-rock composition after linear mixing is calculated:

$$C_{\text{wr}} = C_0(1-X) + C_1X \tag{B1}$$

where X is the melt fraction added to the residual peridotite, and C_{wr} and C_0 are the new and initial whole-rock compositions, respectively. After addition of a melt with concentration C_l, trace elements are redistributed, assuming that newly formed minerals that crystallized from the melt attain equilibrium with pre-existing phases of the peridotite. The new mode M of phase j can be expressed as a function of X:

$$M_j = M_0(1-X) + X\gamma_j \tag{B2}$$

where γ_j is the crystallization mode. This crystallization mode describes the proportions of new minerals that crystallize from the melt. For the model presented in Fig. 9, γ_{ol} and γ_{cpx} were 0·7 and 0·3, respectively (Elthon, 1992). Using these new mineral modes, the new bulk distribution coefficient, D_{bulk}, can be calculated:

$$D_{\text{bulk}} = \Sigma(Kd^{j/1}M_j). \tag{B3}$$

The concentration in the re-equilibrated cpx after melt addition depends on the modified bulk distribution coefficient and is identical to equation (A4).